A simple framework for agent-based modeling with extracellular matrix

John Metzcar[1,2], Ben S. Duggan[3], Brandon Fischer[1], Matthew Murphy[2], Randy Heiland[1] and Paul Macklin[1*]

[1]Intelligent Systems Engineering, Indiana University, 700 N. Woodlawn, Bloomington, 47408, Indiana, United States of America.

[2]Informatics, Indiana University, 901 E. Tenth Street, Bloomington, 47408, Indiana, United States of America.

[3]Computer Science, Indiana University, 700 N. Woodlawn, Bloomington, 47408, Indiana, United States of America.

*Corresponding author(s). E-mail(s): macklinp@iu.edu;

Contributing authors: jpmetzca@iu.edu; bendugga@iu.edu; brandonfischer99@gmail.com; dmatthewmurphy@gmail.com; heiland@iu.edu;

Abstract

Extracellular matrix (ECM) is a key component of the cellular microenvironment and critical in multiple disease and developmental processes. Representing ECM and cell-ECM interactions is a challenging multiscale problem. While several computational frameworks exist for ECM modeling, they often focus on very detailed modeling of individual ECM fibers or represent only a single aspect of the ECM. Using the PhysiCell agent-based modeling platform, we developed a framework of intermediate detail that addresses bidirectional cell-ECM interactions. We represent a small region of ECM, an ECM element, with 3 variables describing its local microstructure: anisotropy, density, and overall fiber orientation. We place an array of ECM elements to spatially model the ECM in a tissue. Cells remodel local ECM microstructure and in

turn, local microstructure impacts cellular motility. We demonstrate the utility of this framework and the reusability of its core cell-ECM interaction model through examples in wound healing, basement membrane degradation, and leader-follower collective migration. Despite the relative simplicity of the framework, it is able to capture a broad range of cell-ECM interactions that are of interest to the modeling community. Furthermore, in our framework, variables representing the ECM microstructure are available to impact all aspects of cell behavior such as proliferation and death. This presents a wide range of possibilities for future modelers to broadly explore cell-ECM interactions, extending currently available models and enabling rapid modeling of cell-matrix biology without requiring custom modeling code for each interaction. We make this framework available as a free and open source software package at https://github.com/PhysiCell-Models/collective-invasion.

Keywords: extracellular matrix, agent-based modeling, collective migration, stigmergy, fibrosis, cancer invasion

1 Introduction

Extracellular matrix (ECM), the material in which cells live, plays a role in a host of biological process from facilitating cell-cell communication to tissue development and organization. It is composed of proteins which are typically organized into several large families: proteoglycans, laminins, fibronectin, and fibrous proteins which in turn can be further grouped by similar physical and chemical properties [1]. Fibrous proteins include the collagen family of proteins and elastin. The ECM and its properties are formed from multiple interacting fibers, for example, through chemical crosslinking of ECM components [2]. Additionally, the ECM includes signaling molecules and many attachment points for cell-ECM interaction [2, 3]. ECM is diverse with composition dependent biomechanical and biochemical properties that vary greatly across locations within the body [1]. It is a living material, actively maintained and modified by cells such as fibroblasts in wound healing and cancer cells in local invasion [1–3]. While cells generate and maintain ECM, ECM also impacts cellular behavior forming a feedback loop. In particular, the matrix properties density of components can hinder or enhance cell migration depending on cell type [4, 5]. The ECM provides cues for cellular migration (contact guidance) through its fiber orientations [6–11]. For example, Carey et al. observed that fiber alignment induced anisotropic cell morphodynamics and spatial probing, guiding them along the axis of alignment, while noting also that many questions remain unanswered regarding how cells navigate these environments [12]. Furthermore, ECM-based signaling, both through mechcanosensing and cell receptor binding to ECM molecules, can impact cell cycle and death [13]. Cell differentiation can also be impacted by ECM [14]. Overall, changes in ECM

microstructure is associated with disease processes, in particular aspects of cancer progression, cancer metastasis, and scarring [8, 9, 15, 16].

Given the importance of ECM in biological processes, there are multiple models and frameworks for exploring ECM and cell-matrix interactions. See reviews that discuss models in the context of cancer, wound healing, and fibrosis [17–20]. Broadly, modeling efforts can be placed in four categories: discrete force-based, continuous force-based, ECM density, and multicomponent that have both an ECM density and orientation.

Examples of the discrete force-based frameworks include Schülter et al. and Nöel et al. where migrating cells and individual matrix fibers are embodied as agents with direct forces dictating motility and realignment respectively [21, 22]. Macnamara et al. also adopt this paradigm and couple it with a model of blood vessel-cell interactions [23]. Other representations calculate forces over a network of individual spring-like elements. Zhu et al. construct ECM from a hook-and-spring network and Tozluoglu et al. model individual fiber filaments as hook-and-spring networks [24, 25]. Tsingos et al. model a network of ECM fibers as a bead-spring chain model and couple this with a cellular-Potts agent-based model [26].

Continuous force-based models represent ECM as a continuously deformable material. Examples include van Oer et al., who use a finite element model of ECM coupled with a cellular-Potts model of cells and look at how stiffness and deformability of the ECM impact cell migration [27]. Ahmadzadeh et al. use a stress-strain relationship to deform fibers and incorporate cell adhesions to investigate cellular level motility and morphology [28].

ECM density approaches often use partial-differential equations (PDEs) to update ECM density. Anderson and Chaplain use a continuous approach that leads to hybrid-discrete continuous approach to study the interplay between angiogenesis and ECM [29]. Zeng et al. use a fibronectin "concentration" in developmental biology applications [30]. Daube et al. use a PDE for a scalar ECM density field in the context of sprouting angiogenesis in tumors [31]. Trucu et al. model invasion as a moving boundary problem with ECM represented as a scalar field [32]. Building off that work, Shuttleworth et al. add non-local effects as well as orientation to the underlying boundary of tumor invasion and adds matrix degradation respectively [33, 34]. Gonçalves and Garcia-Aznar represent the ECM as a density and use experimental migration data to explore tumor spheroids [35]. Lastly, Ruscone et al. study cancer invasion using PhysiBoSS [36, 37], an implementation of PhyisCell [38] with the MaBoSS Boolean network simulator [39], with a model incorporating intracellular signaling activated by contact with a bulk ECM [40].

Finally, there are models that explicitly represent fiber orientation or fiber orientation and density. Chauvier et al. and Hillen et al. use transport models to look at ECM [41, 42]. This work was extended by Painter to introduce a macroscopic ECM density and fiber orientation which was then applied to

model tumor invasion [43]. Other authors model ECM directly as a phase in an otherwise typical cellular-Potts model [44] exploring angiogenesis, tumor invasion, and impacts of cytoplasm and nucleus interaction on migration [45–47]. Some authors also form long-range fibers by viewing sets of contiguous points occupied by ECM as fibers. This allows them to more directly represent fiber orientation and length in addition to density [48, 49]. Park et al. use a modified Vicsek (flocking) model [50] to explore contact inhibition of locomotion in the formation of heterogeneous ECM fiber orientations [51]. Suveges et al. use a hybrid agent-based model and two phase continuous-ECM field approach (oriented, fibrous phase and non-fibrous phase) to study collective migration on oriented ECM [52]. Dallon, Sherratt and collaborators have multiple studies on ECM that include a concept of density and orientation and focus primarily on wound healing and scar formation. The models can be split into hybrid models (discrete cells and continuous ECM) or fully continuous models. Examples of the continuous models include reaction-diffusion and integro-partial differential equation models of wound healing [53, 54]. The hybrid-discrete continuous models include a model of ECM fiber reorientation, an extension to include ECM density, and a third extension to include the impacts of time varying transforming growth factor β profiles with all models including ECM contact guidance [55–57]. See also Sherrat and Dallon's review for additional information on this foundational work focused on the study of wound healing [58]. In a later paper, the model is further extended to combine chemotactic and ECM contact guidance, still in the context of wound healing [59]. Finally, in work similar to Dallon, Sherratt, and colleagues, Martinson et al. use a deposition of discrete ECM puncta followed by cellular realignment of the fibers to study collective migration of neural crest cells using both number of ECM puncta and their orientations to alter cell motion [60].

In this work, we draw upon these prior modeling approaches to capture essential aspects of bidirectional, local cell-ECM interactions. After dividing the ECM into volumetric elements that track local ECM density, alignment, and overall anisotropy (which we refer to collectively as local microstructure), individual cell agents can locally remodel each of these properties, while these properties can in turn influence cell behavior including changes in migration speed, chemotactic response, ECM contact guidance, proliferation, death, secretion, and differentiation. The ECM representation is a mesocale approach that spans between a coarser ECM density field (potentially with sophisticated modeling of viscoelastic mechanics) and more finer-grained approaches that might represent each fiber. We implement this as a framework that can be readily used to incorporate local ECM effects into agent-based models, pairing it with the open source package PhysiCell [38]. To demonstrate the versatility of the framework, we present three sample models focused on local degradation, deposition, and reorientation of matrix and accompanying changes in cell migration. In the first example, we model wound-related fibrosis where activated fibroblasts generate a region that cells cannot enter or leave. In the second, recruited fibroblasts degrade a basement membrane and allow a

tumor to progress from *in situ* growth to local invasion. The third is a model of collective migration which can produce both stigmergy (indirect coordination of migration through changes in their environment) and leader-follower migration, with more aggressive leader cells enabling mixed clusters of cells to invade surrounding tissue. Overall, our framework builds on previous work and is especially inspired by Dallon et al. [55], who developed a model of cell-ECM interactions that were focused on wound healing. We generalized this into an extensible framework that can be rapidly adapted to new problems in particular through use of emerging rules-based formulations [61].

We present our work as follows: Section 2 introduces the ECM representation and cell-ECM interactions and implementation details. Sections 3.1, 3.2, and 3.3 present the example models. Section 4 discusses findings and limits of framework and presented modeling efforts. Our supplemental material cover the cell-ECM interaction model in detail as well as details of cell-cell and cell-environment mechanics [38], PhysiCell rules [61], and sample model parameters.

2 Methods: Framework description

In this section, we first provide the conceptual background and formulation of the ECM and cell-ECM interactions framework (the ECM model). Then, we illustrate the framework with a series of computational experiments highlighting important aspects of the framework. Finally, we give an overview of the computational details.

2.1 ECM and cell-ECM interaction models

To enable explorations of ECM mediated cellular communication and interactions, we developed a three variable ECM representation (orientation, anisotropy and density) and interaction rules for cells and the ECM. We use an agent-based approach to represent cells and a continuum model to represent the fine structure of ECM. Broadly, individual ECM elements are locally remodeled, or modified, by cell migration and ECM production and degradation and in turn, cell motility is impacted by ECM element variables. Overall, the ECM can function as a barrier to cell movement as well as a medium for cell-cell communication with cells modifying the local ECM microstructure to create a readable signal that in turn influences the motility of other cells.

2.1.1 Extracellular matrix representation

Our model is intended to capture key aspects of a small region, or element, of ECM. We conceive of an element of ECM as having three variables: an average fiber orientation (*orientation*), a relative local fiber-fiber alignment

correlation (*anisotropy*), and a quantity that captures the relative amount of material present in an element (*density*). Assembling many of these elements together makes a whole ECM. Figure 1a shows an ECM, which is comprised of tiled ECM elements. The inset shows a single element. It is conceived of as containing many fibers (for illustrative purposes, shown as grey line segments). However, the individual fibers are unmodeled and instead an ensemble of fibers are represented through an average orientation and anisotropy (the black double-headed arrow and its length) and volumetric density (illustrated as number of fibers per element in the schematic).

Mathematically, we center an element at a location $\mathbf{x}$ in space and define them as follows:

- ***Orientation:*** $\mathbf{f}(\mathbf{x})$, the average local fiber direction, represented as a unit length three-dimensional vector
- ***Anisotropy:*** $a(\mathbf{x})$, average local fiber-fiber alignment correlation (range 0 - 1). At zero, there is no correlation and at one, locally there is complete fiber-to-fiber correlation
- ***Density:*** $\rho(\mathbf{x})$, volume fraction of fibers, which we will refer to as the average local fiber density (range 0 - 1). Zero refers to completely fluid-filled and one to completely packed with fibers without void space.

Without a loss of generality, for our simulations and implementation, we arrange the elements in a Cartesian grid.

2.1.2 Cell-based modeling framework

We use the PhysiCell tissue modeling system as our ABM framework, with the ECM model written as an extension [38]. PhysiCell uses a center-based, off-lattice representation of cells and implements physical cell-cell mechanics. It takes a phenotypic approach to encoding cell behaviors letting each cell-agent carry its own parameters and behaviors. Additional details of the mechanics and rules used in PhysiCell are in Supplemental Material Sections 7.3 and 7.4 respectively. To model the diffusive microenvironment, we use BioFVM, which comes with PhysiCell. BioFVM is a diffusion solver that uses a Cartesian representation of space and finite volume method to efficiently handle multiple diffusing substrates over tissue scale sized domains [62].

2.1.3 Cell-ECM interactions

We also model interactions between cells and the ECM. The conceptual model is below with the detailed mathematical model provided in Supplementary Material Sections 7.1 and 7.2.

ECM impacts cell migration (Figure 1b):

- Fiber orientation provides directional cues.

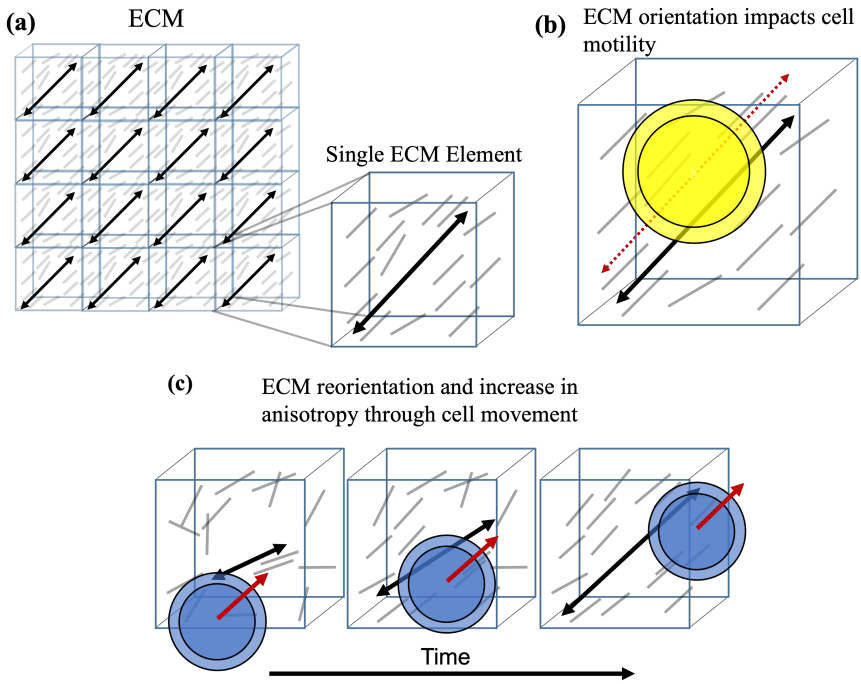

Fig. 1: **Schematic of ECM model and ECM based communication 1a** Illustration of ECM, composed of tiled ECM elements. We conceive of a element of ECM as containing many fibers. However, rather than modeling each of those fibers, we instead model the ensemble, or mean, properties of the set of fibers in a given volume. For illustration purposes, we show a single element containing many fibers (grey line segments) which we quantify by an overall (average) fiber orientation and amount of self-alignment, or anisotropy (the black double-headed arrow and its length). **1b** An element's overall fiber orientation impacts a cell's motility, providing a preferred angle of travel through the element (dashed red arrow). The degree of influence is related to the amount of anisotropy and the cell's ability to sense and respond to the ECM cues. **1c** Cell movement (cell direction - red arrow) remodels ECM by aligning its element's orientation and anisotropy. Cells align an element's orientation parallel to their direction of travel and increase anisotropy proportional to cell speed.

- Anisotropy gives a strength of directional cue: high anisotropy increases an ECM element's influence on direction of cell migration.
- Density influences cell speed: too little ECM, cells have nothing to attach to; too much, cells cannot pass.

Cell migration and movement impact microstructure (Figure 1c):

- Direction of cell migration reorients an ECM elements's orientation.
- Cell-ECM element contact increases ECM anisotropy proportional to cell speed.
- Cells remodel ECM density towards a target value.

This model is motivated by findings in the developmental, disease, and tumor biology literature as well as inspired by previous modeling efforts [1, 8, 9, 55, 63]. The cell-ECM interactions are specified at the cellular level, enabling a variety of cell-ECM interactions, in particular changes in cell motility and ECM

remodeling capabilities [6, 9, 63]. Additionally, ECM variables can be used to impact other cellular behaviors such as proliferation and death. Finally, we note and will demonstrate that these features can be integrated with others such as sensitivity to chemical cues and cell-cell adhesion to obtain an even richer range of cell behaviors.

2.2 Individual features of the cell-ECM interaction model

In this proof of concept section, results isolate and demonstrate a single or small number of aspects of the cell-ECM interaction model presented in Section 2.1. To aid in isolating only ECM-to-cell and cell-to-ECM effects, we disabled cell-cell mechanical interactions by setting cell-cell adhesion and repulsion (C_{cca} and C_{ccr} in Supplemental Material Equations 21 and 23 respectively) to zero. We used multiple cells per result to highlight the uniformity of interactions across the computational domain and as a visual aid rather than to explore how cell-cell interactions may impact the simulations.

2.2.1 Cells produce signals in the ECM

Combing the ECM: Local ECM fiber orientation and alignment remodeling produces extended paths in the ECM

Remodeling of the ECM units can produce paths that ECM sensitive cells can then follow. In Figure 2a, a column of cells move deterministically from left to right across a field of un-oriented ECM aligning it in the direction of travel. Each ECM element is initialized with a random orientation and uniformly with $a = 0.9$. Remodeling cells move across the domain, producing individual changes in ECM elements as they travel. After four passes of modifications, or writing signals, to the matrix, the ECM is aligned almost completely parallel to the direction of travel with the additional effect of a slight increase in anisotropy, demonstrating ECM reorientation and producing preferred paths of transit across the domain. Note that we run this simulation in 2-D to aid in visualization and to demonstrate uniformity across the domain. A video is linked in the Supplemental Material (Section 7.6).

2.2.2 Cells read signals in the ECM, impacting their migration

All results in this section were produced with anisotropy and density uniformly set to 1.0 (maximum and most impactful value) and 0.5 (value of maximum cell speed ρ_{ideal} from Supplemental Material Equation 7.2.2) respectively and with both the chemical and physical (ECM) environments held constant. This ensures that only dynamics between a cell and the ECM or respectively among a cell, ECM, and chemical field impact the results. Finally, the cells are highly sensitive to ECM ($s = 1.0$ from Supplemental Materails Equation 9) as well

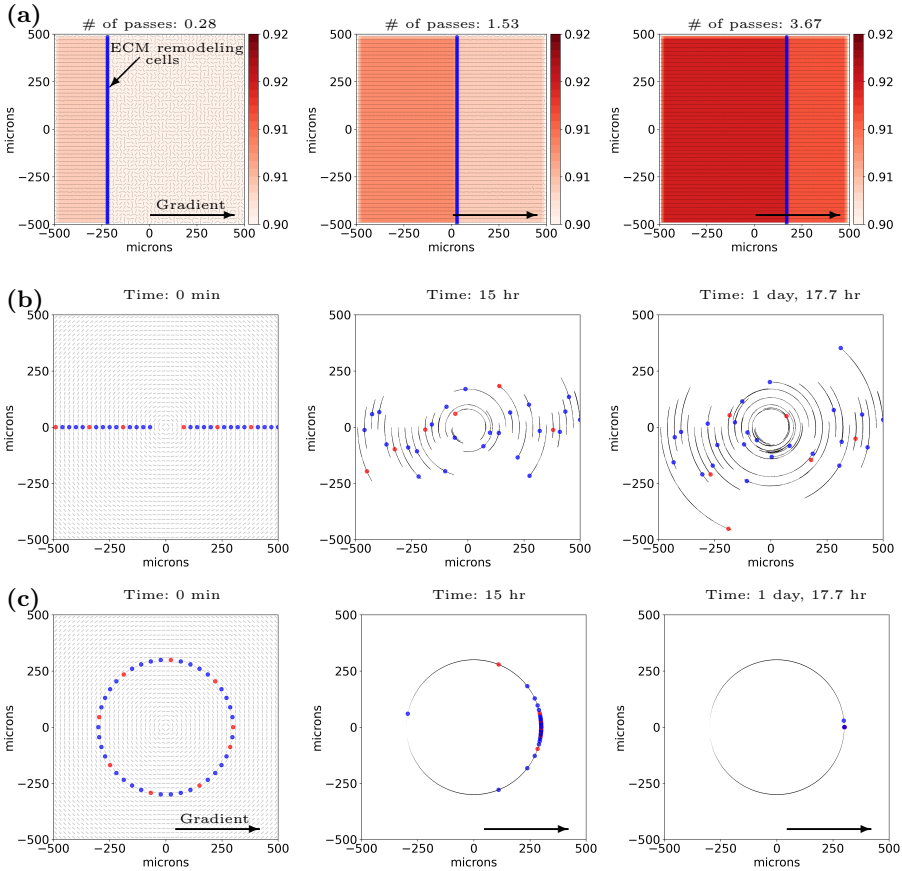

Fig. 2: **Highlights of individual aspects of the cell-ECM interactions:** (**2a - Remodeling**) A line of ECM remodeling cells (blue circles), motivated by a constant chemical gradient (black arrow), move in the positive x-direction, reorienting an initially random field of orientations (black line segments) with uniform anisotropy of 0.90 (left-most image in **2a**). Upon reaching the simulation boundary, the cells reset to the opposite boundary, and remodeling continues (middle - 2 passes). At four passes, each ECM element is almost completely reoriented parallel to the direction of travel of the cells and anisotropy has increased from 0.90 to ∼0.92 (right), in particular demonstrating the framework's ability to reorient ECM elements. Note that we run this in 2-D to aid in visualization and demonstrate uniformity across the domain. **2b, 2c - Reading ECM**. Both simulations use ECM elements that are highly anisotropic (a uniformly set to 1.0) and element orientations arranged to form approximate concentric circles. The simulation in **2b** begins with ECM sensitive cells almost equally spaced along the line y=0 (leftmost image - cells shown in red and blue; color is for visual contrast only). Cells follow the ECM circles in an approximate 1-D random walk due to ECM following and without need for further motility rules, forming circular arcs (small black arrows marking cell position history every 6 minutes). As the rate of curvature of ECM cues decreases away from the center of the computational domain, the cells better follow the ECM circles. The simulation in **2c** contrasts with **2b** by providing an additional environmental cue - a chemical gradient. As the ECM sensitive cells integrate both signals, in contrast to **2b**, their motion is no longer random and they travel uniformly in the direction of the gradient. With a circular initial configuration (left), the cells follow each other along the same circle (middle and right), coming to a point of relative stability where the ECM orientation is exactly perpendicular to the chemical field. Note that the ECM is static in **2b** and **2c** and does not vary across time. Videos are available. See the following links 2a, 2b, and 2c.

as to the chemical gradient ($b = 1.0$ from Supplemental Material Equation 15) when present.

Cells can closely follow paths in the ECM

Supplementary Figure 3 shows influence of ECM on cell migration combined with a chemotactic field going to the right. The leftmost subfigure shows the initial cell positions as well as the ECM element fiber orientations (45° and -45° from the x-axis in the top and bottom sections of the domain respectively). Without ECM influence, the cells would simply move to the right. Instead, the ECM biases the cell paths away from the path set by the gradient. The middle and rightmost images include the cell's positional history, shown as arrows trailing the blue and red cells (note in this and in all images in this section, the cell color is simply for visual contrast). A video is linked in the Supplemental Material (Section 7.6).

Cells perform approximate 1-D random motion along ECM paths

Figure 2b shows the results of cell motion on circular ECM. We show the initial cell configuration as well as the ECM element orientations on the left with the middle and right images including cell positional history at 15 hours and 41.7 hours simulated time respectively. Our ECM model does not encode a preferred direction, so as expected, we observe approximate 1-D random motion along the ECM circles in this proof of concept simulation. Because of the curved tracks and discretization error in highly curved regions (center of domain in this case), contrasting with Supplementary Figure 3, some cells move off their initial paths out to ECM circles of higher radius. We expand on this phenomena in the discussion (Section 4). Due to the high discretization error at the center of the domain, for this simulation, we exclude the central region with radius of 80 μm or less. A video is linked in the Supplemental Material (Section 7.6).

Cells can integrate environmental signals and follow non-linear paths

Figure 2c shows the results of cell motion transiting circular ECM with an additional cue supplied by a chemical gradient. This additional information causes the cells to follow the ECM circle on which they were initially placed to the right (the direction of the chemical gradient). Note that at locations where the chemical gradient and ECM orientation are perpendicular, cells are in a quasi-stable state as the two directional cues cancel. This meta-stable state is seen in the lagging cell in the middle plot of Figure 2c. Note that all other cells in this plot, except the lagging blue cell on the left side of the image, have moved many cell lengths from their initial positions. This cell began at the x-axis, which defines a line in which all units of ECM have an orientation

perpendicular to the chemical field. Likewise, all the cells converge at the x-axis, where their initial ECM contour becomes perpendicular to the chemical field. Unlike in Figure 2b, with cells placed further from the origin and in a region of lower curvature, we do not observe "track jumping". A video is linked in the Supplemental Material (Section 7.6).

2.3 Computational method details and data availability

This work is implemented and run in PhysiCell 1.12.0 [38]. It also uses the recently introduced PhysiCell rules [61]. All code is available with a permissive BSD license, including the ECM extensions and sample models, at GitHub with the latest release located here. The code is cross-platform capable and has been tested on Ubuntu 22.04, Windows Server 2022, and MacOS 12. All simulation data for this paper is available for download at Zenodo. A free, interactive cloud-hosted version of the collective migration model, using the ECM and cell-ECM frameworks, is available at nanoHUB (note - sign up is required).

On consumer-grade hardware (2019 Macbook Pro), typical wall times were 13 minutes for the longer fibrosis simulation and 10 minutes for the invasive carcinoma and leader-follower simulations. On high-performance computing hardware, mean wall times were 4 minutes for the fibrosis simulation and 3.2 minutes for the invasive carcinoma and leader-follower simulations. The simulations start with 412 (fibrosis), 517 (invasive carcinoma) and 703 (leader-follower) cells and simulate 15 days, 10 days, and 10 days respectively. The fibrosis model decreases agents as the simulation proceeds but also simulates 50% more time, hence its longer run time.

We conducted stochastic replicates for the main examples. To ensure that simulations within each example began with the same initial configuration (in particular in the collective migration example), we begin the simulations with the random number generator seed set. As such, stochastic replicates were achieved by exploiting multi-threading to produce unique update orders and simulation trajectories.

We performed initial model exploration using DAPT 0.9.2. DAPT is a straightforward way to organize model exploration on a mixed compute resources for small teams. For more information see Duggan et al. [64].

We used xml2jupyter to transform this command line C++ code into a Jupyter notebook-based graphical user interface [65]. This version is the interface deployed at nanoHUB.

3 Framework examples: Fibrosis, basement membrane degradation, and collective migration

We present three modeling vignettes to demonstrate framework features and ability to represent a range of biological phenomena, focusing on ECM remodeling and cell motility. To help isolate dynamics due to physical interactions and cell motility, the presented examples do not include cell proliferation and death (except where required) as features. We use the default cell definition from PhysiCell, varying relevant parameters and behaviors as noted in each example. To examine the robustness of the simulations to stochastic variation, we ran each primary model 20 additional times over what is reported here and qualitatively compared across model runs.

For the chemical microenvironment, we use default settings unless noted otherwise. We pre-condition the domain by running the diffusion solver for 10 simulated minutes before starting the simulation. For ECM, we use the model described in Section 2.1. We place the ECM elements overlaying the BioFVM voxels exactly; the two meshes have a shared origin and coordinate system. See each example for exact microenvironment set up.

Finally, we note that the models were developed and are presented as a 2-D simulation (single slice of a 3-D environment).

3.1 ECM deposition (fibrosis) and enclosure of a wound

We produced a simple model of fibrosis. We model the recruitment of cells to clear an injury - first macrophages and subsequent recruitment of fibroblasts to rebuild the ECM in the area of the injury [16, 66, 67]. Fibroblasts are activated in the presence of macrophages, depositing ECM, leading to formation of a barrier and subsequent exclusion of cells from the wounded area.

Model results and cellular behaviors

We use three cell types - distressed/dead cells, macrophages, and fibroblasts similarly to [68]. The key rules of the model are summarized in Table 1. Broadly, the distressed cells die immediately and release debris after having already begun to release debris prior to dying (Figure 3a). This is similar to an injury or some other insult that could cause a small region of cells to die at once. The debris recruit macrophages (shown in red) which chemotax up the debris gradient. Upon reaching the damaged cells, macrophages phagocytose the dead cells and also send out an inflammatory signal to initiate additional tissue repair. This signal recruits fibroblasts (yellow) via chemotaxis, which attempt to repair the damaged tissue by secreting ECM materials (increasing density) (yellow-to-red filled contours) as seen in Figure 3b,c,d. As fibroblasts

Table 1: **Fibrosis model:** principle behaviors, parameters, and systems effects

Cell type	Behavior	Key parameter(s)	Key outputs
Distressed cells	Secrete debris	Debris secretion rate	Recruits macrophages to dead cells
	Death	NA - cells die immediately at start of simulation	Begins fibrotic cascade
Macrophages	Chemotaxis up debris gradients	Bias	Enables macrophages to find dead cells
	ECM density response	-	Cell speed is reduced as ECM density moves away from ideal value (0.5)
	Consume debris	Debris uptake rate	Aids in generating gradient
	Consume dead cells	Dead phagocytosis rate, phagocytosis rule saturation value and half-max	Enables clearance of cells
	Secretion of inflammatory signal	Signal rule saturation and half-max values	Recruits fibroblasts to region of damaged cells
Fibroblasts	Chemotaxis up inflammatory gradients	Bias	Enables fibroblasts to find macrophages
	ECM density response	-	Cell speed is reduced as ECM density moves away from ideal value (0.5)
	Degrading/depositing ECM density	ECM density target value; ECM density secretion rule saturation and half-max values	Can trap cells if deposited at high enough amount

and macrophages remain in contact, ECM continues to be produced. This eventually leads to the entrapment of the recruited cells. As the dead cells continue to shrink due to their death process, a relatively fluid-filled region, or cyst, forms enclosed by a layer of impenetrable ECM (Figure 3e,f). See the Supplemental Material Table 4 for additional details. A video of results presented in Figure 3 is linked in the Supplemental Material (Section 7.6).

Of the 20 stochastic replicates, 14 generated a completely enclosed region with 6 resulting in a partial enclosure. See the simulation data set at Zenodo for individual results.

Tissue microenvironment

We use two diffusive chemical fields in this simulation. Debris is emitted by distressed and dead cells and has a very small diffusion coefficient, representing the slow movement of cellular debris and no decay on the simulated time scales (macrophage consumption is the only removal process). This field represents

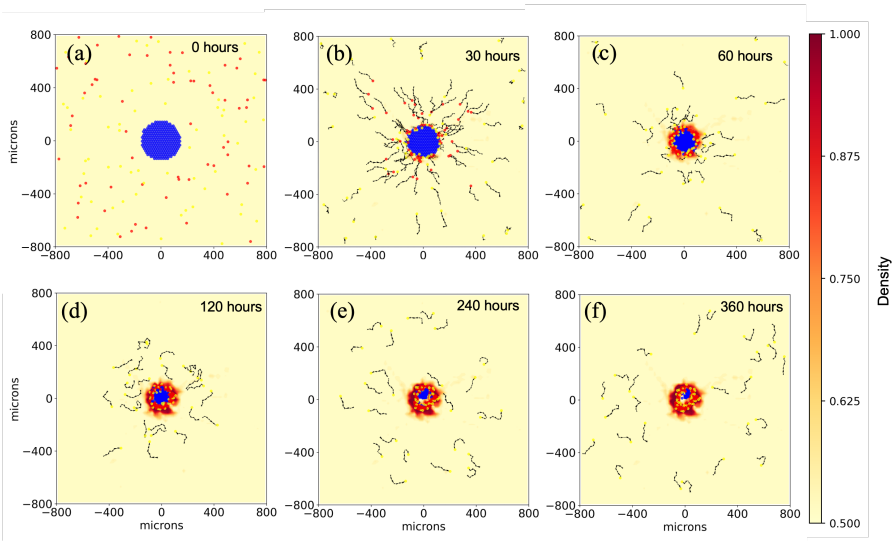

Fig. 3: **Fibroblast ECM secretion leads to cyst formation:** Tissue injury, modeled as sudden death of a number of cells (blue cells) attracts macrophages (red) to remove dead cells (a, b). The macrophages recruit fibroblasts (yellow), which secrete ECM as part of the tissue repair process (c, d). However, prolonged contact with macrophages leads to continued secretion of ECM density. This produces a region of impenetrable ECM which both traps the macrophages and fibroblasts and leads to a region that is relatively fluid-filled as the dead cells continue in their death process. Initial configuration - dead cells 175 μm circle with macrophages and fibroblasts randomly placed outside of the distressed region. Yellow cells: fibroblasts. Red cells: macrophages. Blue cells: distressed/dead cells. Yellow-to-red contour plot: ECM density. Black arrows: cell positional history, going back eight time points (sampled every 30 minutes). This is available as a video. See link here.

the materials that distressed and dead cells release as part of the death process. We also simulate an inflammatory signal, released by macrophages as part of their response to contact with dead cells. It has a characteristic length scale of 32 μm, or approximately 2.5 cell diameters. Both fields have no flux conditions.

The ECM density begins at the uniform value of 0.5 and anisotropy of 0. Fibroblasts modify the density when recruited by macrophages. We note that in this simulation, only ECM density impacts cell motility, as the motile cell populations are modeled as being insensitive to ECM orientation cues.

See the Supplemental Material Tables 5 and 6 for additional details.

Tissue

Distressed cells are placed at the center of the computational domain in a circular region of radius 175 μm. Cells are initialized at approximate equilibrium spacing with six neighbors (hexagonal packing). Fibroblasts and macrophages are placed randomly throughout the domain, excluding the 200 by 200 μm square containing the distressed cells, with placement of all cells held consistent across stochastic replicates. See the Supplemental Material Table 7 for additional details.

Comparison to previous modeling efforts

Comparing to previous work in the field, Dallon et al. 2001 studied the impacts of TGF-β on collagen deposition in wound healing [57]. In their model, fibroblasts deposit collagen (ECM density) in response to TGF-β. Comparing results between baseline TGF-β and increased TGF-β, they find more collagen deposition resulting in slower agents and less penetration of cells into the wound. While caused by a different dynamic (concentration of a signaling molecule versus contact with a different cell type), this is comparable to the slowing of the fibroblasts as they increase ECM density followed by the inability of them to penetrate fully to the center of the wound. Note also that in this simple example, we are not modeling contact guidance whereas Dallon et al. do [57].

3.2 Basement membrane disruption precipitating transition from *in situ* to invasive carcinoma

Here, we model the transition from a ductal carcinoma *in situ* to invasive carcinoma. Cancer cell recruited fibroblasts degrade basement membrane (represented as high density ECM) enabling subsequent cellular invasion [8, 69, 70].

Model results and cellular behavior details

In this model, there are two cell types - cancer cells and fibroblasts. The key rules of the model are summarized in Table 2. In this case, we simulate the duct's longitudinal cross section. We start with an outgrowth of cancer cells (half circle of blue agents). The cells have grown into the fluid-filled region of low ECM density - the duct lumen. They are on a band of very dense ECM ($\rho = 1$ - dark horizontal band in Figure 4a) which represents the duct's basement membrane. The basement membrane is surrounded by stroma - with density of 0.5 (Figure 4a). The cancer cells emit a tissue remodeling factor, modeled as an inflammatory factor, that attracts fibroblasts via chemotaxis with high bias (field not visualized). The fibroblasts alter the ECM and basement membrane, increasing anisotropy in the stromal region and degrading the basement membrane as they move into the tumor (Figures 4b, c, and d). Due to close contact with fibroblasts, cancer cells become more mesenchymal, altering their adhesion and affinity to each other, and escape following the oxygen gradient coming from the bottom of the simulation (Figures 4e, f). Because the cancer cells follow ECM, they preferentially move along the groomed ECM paths, or portions of high anisotropy, but also transit the ungroomed ECM in their movement out of their location of origin (Figures 4g,i). See the Supplemental Material Table 8 for additional details. A video of results presented in Figure 4 is linked in the Supplemental Material (Section 7.6)

Table 2: **Invasive carcinoma model:** principle behaviors, parameters, and systems effects

Cell type	Behavior	Key parameter(s)	Key outputs
Cancer cells	Secrete inflammatory signal	Secretion rate, target value, and secretion rule parameters	Recruits fibroblasts
	ECM following	ECM sensitivity	Enables invasion of stroma
	ECM density response	-	Cell speed is reduced as ECM density moves away from ideal value (0.5)
	Chemotaxis up oxygen gradients	Bias	Enables escape
	Decrease in cell-cell adhesion on contact with fibroblast	Adhesion rule saturation and half-max values	Enables cells to more readily escape the tumor mass
	Decrease in cancer cell affinity on contact with fibroblast	Affinity rule saturation and half-max values	Enables cells to more readily escape the tumor mass
Fibroblasts	Chemotaxis up inflammatory gradients	Bias	Enables fibroblasts to find cancer cells
	ECM density response	-	Cell speed is reduced as ECM density moves away from ideal value (0.5)
	Degrading/depositing ECM density	ECM density target value	Removal of barriers to cell movement
	Altering ECM orientation and fiber-fiber alignment	ECM reorientation rate and anisotropy growth rate	Provides paths for cell escape
	Decrease speed on contact with cancer cells	Speed inhibition rule saturation value and half-max	Slows cell speed enabling remodeling to occur

All 20 stochastic replicates generated qualitatively similar results - basement membrane degradation and subsequent invasion of stroma. See the data supplement for individual results.

Tissue microenvironment

We use two diffusive chemical fields in this simulation. Inflammatory signal is emitted by the cancer cells and has a diffusion length scale of 100 μm in regions of high fibroblast density. We also simulate a nutrient field, modeled as oxygen (length scale of 1000 μm in open tissue and 100 μm in cell dense regions) coming in to the duct from the bottom of the simulation. The inflammatory signal has no flux boundary conditions while the oxygen has a constant value (Dirichlet condition) at the bottom of the domain and no flux conditions at the other boundaries (mixed conditions).

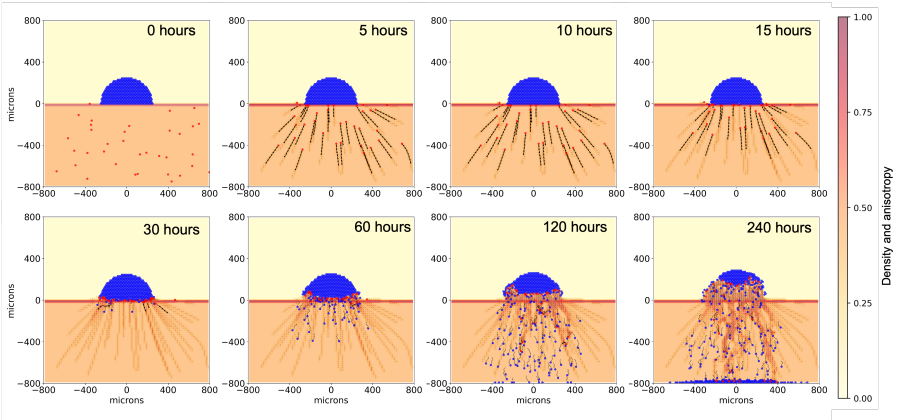

Fig. 4: **Dense ECM can form barriers while ECM remodeling can lead to cell invasion:** Beginning with a fluid-filled lumen, a layer of dense, impenetrable ECM, and stromal tissue, we see that ECM modifying fibroblasts remodel the tissue locally, enabling the cell escape out of a growing carcinoma and into surrounding tissue. Initial configuration - cancer cells in half circle with 175 μm circle with fibroblasts randomly placed outside duct. Red cells: fibroblasts. Blue cells: cancer cells. Yellow-to-red contour plot: ECM density and anisotropy (alpha = 0.5). Black arrows: cell positional history, going back eight time points (sampled every 30 minutes). This is available as a video. See link here.

The ECM begins with three zones. The top of the simulation, in which the cancer cells start, represents the interior portion of a duct (the lumen). We model it as completely fluid-filled with ECM density set to zero. The duct is surrounded by a region of very dense ECM which represents the basement membrane. Finally the duct itself is surrounded by stroma, which we model with an ECM density of 0.5. We are viewing the duct in a longitudinal cross section, rather than axial.

See the Supplemental Material Tables 9 and 10 for additional details.

Tissue

Cancer cells are placed in the upper half of the domain in half circular region of radius 175 μm with its main diameter in contact with the region of dense ECM (basement membrane). Cells are initialized at approximate equilibrium spacing with six neighbors (hexagonal packing). Fibroblasts are randomly placed throughout the lower portion of the domain, with placement held consistent across stochastic replicates. See the Supplemental Material Table 11 for additional details.

Comparison to previous literature

Comparing to previous modeling results, Kim and Othmer investigated stromal invasion enabled basement membrane degradation [71]. In their model, also inspired by DCIS, the tumor cells themselves degrade the basement membrane by secreting protolytic enzymes. They observed that a front of leading cells

Table 3: **Cell-based model:** principle behaviors, parameters, and systems effects

Phenotype	Behavior	Key parameter(s)	Key outputs
Leader cells	ECM remodeling	Cellular rate of matrix realignment, rate of anisotropy growth	Lays cues for followers to sense
	Chemotaxis	Bias	Enables production of coherent paths
	Cell-cell adhesion and repulsion	Ratio of adhesion strength to repulsion strength	Enables collective cell migration
Follower cells	ECM following	ECM sensitivity	Allows cells to use cues in the ECM
	Chemotaxis	-	Enables coherent migration
	Cell-cell adhesion and repulsion	Ratio of adhesion strength to repulsion strength	Enables collective cell migration
	Random motion	-	Enables finding of paths in the ECM

form as the basement membrane was broken down compared to our more dispersed breakdown of basement membrane and invasion. However, they had a point source of attractant compared to our line source. Furthermore, our basement membrane is broken in several locations and our tumor cells follow contact guidance. Both of these features tend to promote a spreading of the tumor cells compared to Kim and Othmer's scenarios. Regardless, in each case, the breakdown of the ECM surrounding the mass of cells lead to cellular invasion [72].

3.3 ECM contact guidance enables leader-follower migration

To address questions centered on the mechanisms of multicellular invasion, we developed a tissue simulation focusing on collective cell migration. It is inspired by the cancer biology literature [63, 73] and builds off previous cell-based spheroid modeling work [38]. Mimicking Cheung et al., we include two cell phenotypes: more aggressive leader cells and less aggressive follower cells. Their observations suggest some form of communication between the leaders and followers; we model that communication as signals written in and read from ECM microstructure. We use our cell-ECM interaction model with leaders writing signals (remodeling microstructure) and followers reading those signals (contact guidance). Simulating these indirect cellular interactions lets us explore and test for the microenvironmental conditions and behaviors that may be required for ECM mediated collective migration. Model details follow as well as more detailed accounting of the simulations that lead up to collective migration.

3.3.1 Leader-follower model details

Cellular modeling

We model two different phenotypes - leader cells and follower cells. In our example, these cells represent invasive and non-invasive cancer cells, respectively, but they could represent other types of cells that exhibit similar behaviors (more motile and less motile sub-phenotypes). The key rules of the leader-follower model are summarized in Table 3. In particular, leader cells follow oxygen gradients with a high chemotactic bias and encode their movements via ECM remodeling (see Section 7.1 for mathematical details). Followers' movements are influenced by signals in the ECM (contact guidance) and are chemotactic with bias equal to local value of a (Chemotaxis Model II - Equation 16) following previous works that used chemotactic bias [59, 60]. They read signals in the ECM with a high sensitivity ($s = 1.0$) and are incapable of remodeling ECM. Thus, in highly anisotropic ECM, followers use contact guidance and chemotax, while in unaligned ECM, they move randomly. Overall, leaders alter the ECM microstructure, providing a preferred route through the ECM for followers to read by contact guidance, effectively communicating or signaling paths to follower cells. See the Supplemental Material Table 12 for additional parameter values.

Tissue microenvironment

We simulate avascular tissue with a diffusing oxygen-like field coming from the domain boundaries (Dirichlet conditions). Cells uptake oxygen and there is decay in the cellular milieu. As in the basement membrane example, we use a diffusion length scale of 100 μm for regions of high cell density. See Supplemental Material Table 13 for additional details.

The ECM is initialized uniformly with anisotropy of 0.0, ECM density of 0.5 (no impact on cell speed), and random fiber orientations. See Supplemental Material Table 14 for additional details.

Tissue

Cells are placed at the center of the computational domain in a circular region of radius 175 μm and were randomly assigned to be either followers or leaders (95% followers, 5% leaders). Cells are initialized at equilibrium spacing with six neighbors (hexagonal packing). See the Supplemental Material Table 15 for additional details.

3.3.2 Leader-follower results

Signal generation and reading are required for collective behavior

We begin the exploration as a proof of concept with simplified dynamics: leader cells exhibit the limit or extreme behavior of instant ECM microstructure remodeling, using Supplemental Material Equations 1 and 2. (The previous examples, Sections 3.1 and 3.2, used continuous or non-instant remodeling - Supplemental Material Equations 3 and 5.) We use these simplified dynamics to aid exploration, not to suggest that cells necessarily modify ECM much faster than they move and eventually relax this extreme. Additionally, to show there is impact from the cell-ECM interactions, we isolate two model rules, the ability to produce and read signals, while disabling cell-cell adhesion. In Figure 5, we observe similar results with ECM writing only (left column: follower ECM sensitivity s set to zero) and ECM reading only (middle column: leader remodeling rates set to zero). In both cases, leaders separate from the initial disc of cells and reach the simulation boundary around 16 hours while followers remain roughly in the center of the domain. Only with both writing and reading (right column) were most cells able to escape the domain center and invade their surroundings. The guidance provided by the ECM combined with the chemotactic behavior of followers on groomed ECM enables them to follow the leaders' paths out of the center of the domain, resulting in stigmergy, wherein agents alter their environment effectively communicating preferred paths to other agents. Links to simulation videos are in Section 7.6.

Note that we hold the initial configuration of each simulation variation constant to isolate motility effects only.

Cell-cell adhesion enables collective migration

Adding cell-cell adhesion (see Supplemental Material Section 7.3 for details on the cell-cell adhesion model) to provide more realism to the simulation, yet still using the limit assumption of instant signal writing, we observed a range of dynamics and cellular patterning, including collective migration in which phenotypically heterogeneous cells gather in clusters and move together roughly maintaining the same composition over time. We see that ECM mediated communication can still produce stigmergy (Figure 6a) when speed is high enough to overcome cell-cell adhesion. In Figure 6b, we see leaders migrated to the leading edge of cell cluster. Due to a balance between cell motility and cell-cell adhesion, cells stay in contact with each other, producing leader-follower collective invasion. Finally, when cell speed is even lower, adhesion takes over cell mechanics and cell positions are constant over the computational experiment (Figure 6c). Links to simulation videos are in Section 7.6. Note that cell-cell adhesion is of equal strength across all possible combinations of interactions (follower-follower, follower-leader, and leader-leader). Also, due to our interests in highlighting cell-ECM interactions, we have excluded exploring other

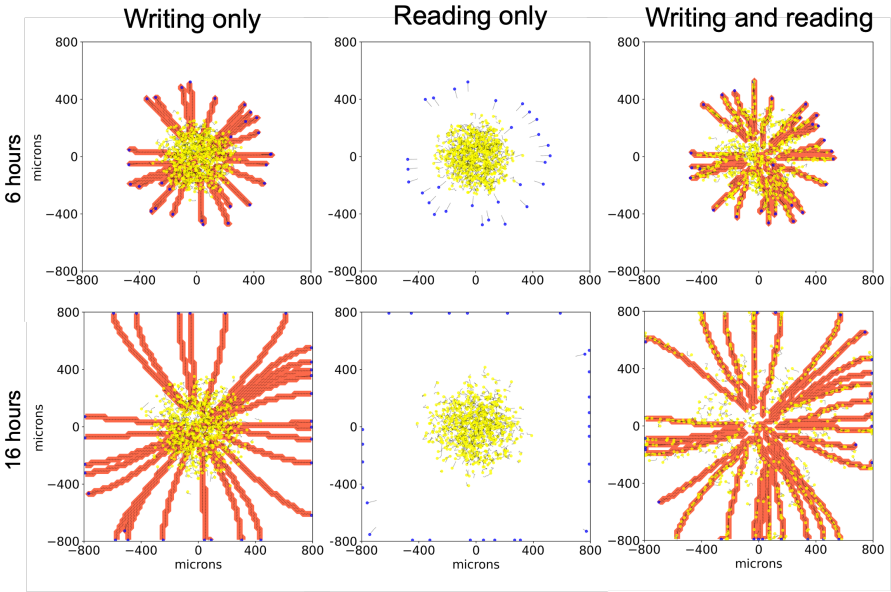

Fig. 5: **Communication of cell path through environmental modification produces stigmergic cell behavior:** Modification of the environment (left) and reading of the environmental signals (middle) separately do not produce collective behavior. With both together (right column) we observe that most cells escape the domain center and invade their surroundings through the combined effects of following leaders' paths (stigmergy) and chemotaxis. Writing only: s, ECM sensitivity, for followers set to zero. Reading only: r_{f_0} and r_{a_0}, reorientation and realignment rates, for leaders set to zero. Initial configuration - 703 agents (5 % leaders) in 175 μm circle. Yellow agents: followers. Blue agents: leaders. Red contour plot: ECM anisotropy - uniformly equal to one in remodeled ECM elements. Line segments: ECM orientation. Black arrows: cell positional history, going back 12 time points (sampled every 6 minutes). Videos are available. See the following links 5a, 5b, and 5c.

possible ways to enable collective migration such as cell-cell repulsion plus cell proliferation but did not explore that in this model.

Collective migration is retained in the context of non-instant signal generation

Having shown that the cell-ECM model can produce a range of behaviors in the limit of instant signal generation, we now relax this limit assumption and let signal generation occur over a period of time instead of instantly. We give ECM reorientation and anisotropy non-instant rates of change and update them with Supplemental Material Equations 3 and 5, as in the previous example models. See Section 7.1 for additional model details. Figure 7 contrasts the results of the limit of instant signal writing with non-instant signal writing. Figure 7a shows two time points using the limit model, with cell speed of 0.5 μm/min and adhesion value of 10 μm/min (the same parameters as Figure 6b). In the earlier time point (top), we see what was the initial cluster of cells broken into several smaller clusters moving out from the center of the domain. In the

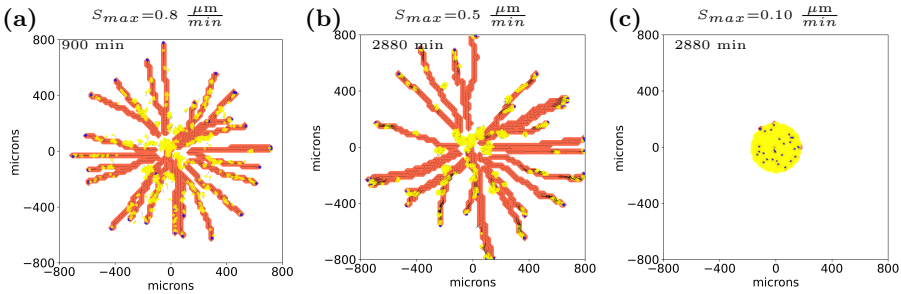

Fig. 6: **Multiple behaviors are produced with the leader-follower model by including cell-cell adhesion:** With cell-cell adhesion on (adhesion = 10 $\frac{\mu m}{min}$ across all cell-cell interactions), multiple behavioral regimes are observed in the limit case of instant remodeling. In **(a)** with S_{max} at 0.8 $\frac{\mu m}{min}$, we see stigmergy with followers (yellow cells) following trails left by leaders (blue cells), as in Figure 5.**(b)** Decreasing S_{max} to 0.5 $\frac{\mu m}{min}$ yields collective migration. In **(c)** with S_{max} at 0.1 $\frac{\mu m}{min}$, cell-cell adhesion cannot be overcome and the cell positions are frozen in the initial configuration. Initial configuration - 703 agents (5 % leaders) in 175 μm circle. Adhesion set to 10 $\frac{\mu m}{min}$. Yellow agents: followers. Blue agents: leaders. Red contour plot: ECM anisotropy - uniformly equal to one in remodeled ECM elements. Line segments: ECM orientation. Black arrows: cell positional history, going back 12 time points (sampled every 6 minutes in **a**, every 30 minutes in **b**, and every 120 minutes in **c**). Videos are available. See the following links 6a, 6b, and 6c.

next time point, we see that heterogenous clusters have continued towards the simulation boundary (with some reaching it) while clusters of followers remain in the middle. In Figure 7b, relaxing instantaneous signal writing, we observe that collective migration still occurs. Leaders remodel ECM with the amount of remodeling, and thus signal strength, depending on residence time and cell speed, leading to a range of anisotropy values. They remain in contact with followers and lead them out of the center of the domain. However, because altering ECM microstructure (in particular increasing anisotropy) is no longer instant, the signals to followers are not as strong compared to 7a. Furthermore, we observe that fewer cells are at the periphery of the domain when remodeling is slower (finite). The relative lack of strong signals in the non-instant scenario leads to less chemotactically biased migration (more random migration) in the follower population, decreasing the uniformity of velocity vectors across a cluster of cells. Thus, as the cells adhere to each other but attempt to move in divergent directions, overall cell speed is effectively reduced. The more uniform the cell velocities, the closer to S_{max} the average speed of a cluster will be. Overall, the lack of uniformity leads to less coherent migration in which the consistently chemotactically-driven leaders break away and are then able to proceed ahead of the followers. For more details see Section 7.3 and Equation 18. The remaining followers then continue out behind the leaders via stigmergic behavior. See Supplementary Section 7.6 for links to videos.

In this sample model, we did not explore asymmetric rates of cell-cell attachment. Spring-like attachments with different rates of attachment versus detachment may better mimic cell-cell adhesion [74]. This enhanced adhesion might enable leaders to better pull cells and produce collective migration, perhaps eliminating the need for the followers' oxygen-driven directional cue.

Additionally, this model could be further explored for jamming effects due to strong, but directionally conflicting ECM paths, in particular in the context of comparing effects of the lock in of local chemotactic gradients with the instant model versus the perhaps smoothing affects of the non-instant model.

Finally, we note that collective migration behavior in the finite signal writing scenario is sensitive to remodeling parameters and is lost with a less than order of magnitude change in fiber realignment and reorientation rates as seen in Supplementary Figure 4. Fiber reorientation and realignment rates varying by a factor of four are enough to change the behavior.

We performed stochastic replicates on continuous remodeling collective simulation (Figure 7b). All 20 stochastic replicates generated qualitatively similar results - leader-follower type invasion followed by continued stigmergic movement of followers along the leader generated ECM paths. See the data supplement for individual results.

Comparison to other works

Comparing to previous biological and modeling work in the field, Ilina et al. studies collective migration and cancer metastasis, focusing on cell-cell adhesion and ECM density. Their experimental results showed that even with low cell-cell adhesion (for example with knocked down E-cadherin expression) and with high ECM density, also corresponding to relatively decreased speed, collective migration could be observed. Furthermore, the phenomena of collective behavior - paradoxically present both with and without high cell-cell adhesion - was investigated with an ABM. In particular, the authors found that low cell-cell adhesion and low ECM density, which led to higher cell speed, was associated with individual cell migration, while high ECM density (lower speed) and sufficiently high cell-cell adhesion enabled collective migration, as was observed in their other results [75]. Overall, these results (both the *in vitro*/*in vivo* and *in silico*) are similar to our results in Figure 6, specifically 6a and 6c respectively. Following up on those results, Kang et al. studied collective cell migration in tumor spheroids with a hybrid vertex-particle-based model, culminating in a phase diagram of cell jamming [76]. They found that in the regime of low cell speed and higher ECM density (more regions of excluded volume within the domain), cells remained clumped together (solid phase) until a sufficient speed was reached to enable a collective movement (liquid phase). Finally, with lower ECM density (relatively less volume exclusion for cells) and higher cell speeds a gas-like phase was observed. Again, these results are similar to our results in Figure 6 with the gas phase corresponding to Figure 6a, liquid phase to 6b and solid to 6c. Interestingly, both [75] and [76] either hint at or produce phase diagrams. Future work with this example model in particular could explore the transitions between the subplots of Figure 6 as a phase diagram.

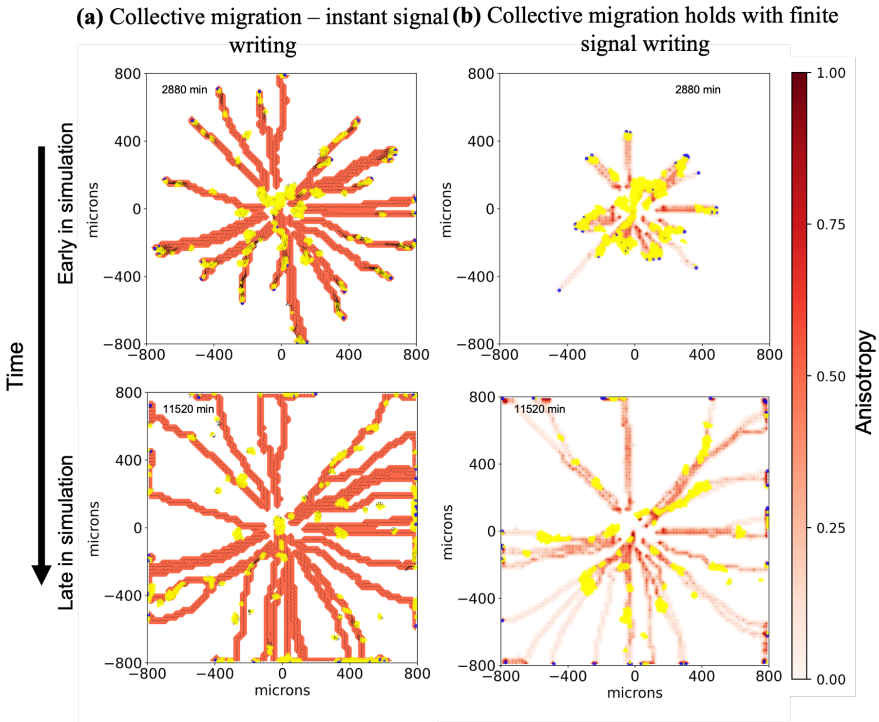

Fig. 7: **Collective migration is retained in the context of non-instant communication** In **(a)**, which is the limit case of instant signal generation with one more time point than Fig 6**b**, we see collective migration with mixed clumps of both leader (blue) and follower (yellow) cells migrating together . As observed in (**7b**), this behavior is robust to non-instant signal writing (modification of ECM variables). Leaders stay in contact with followers and lead them out of the center of the domain. They do not stay in contact as long as in **(7a)** but strong enough paths are generated to enable followers to continue out via stigmergy. This behavior is sensitive to remodeling parameters and is lost with a less than order of magnitude change in them. See Supplementary Material Figure 4. Fiber realignment rate: 0.004 min^{-1}, fiber reorientation rate: 4 min^{-1}. Initial configuration - 703 agents (5 % leaders) in 175 μm circle. Adhesion set to 10 $\frac{\mu m}{min}$. Yellow agents: followers. Blue agents: leaders. Contour plots: ECM anisotropy - (**(7a)**) uniformly equal to one in remodeled ECM elements and (**(7b)** color bar. Line segments: ECM orientation. Black arrows: cell positional history, going back 12 time points (sampled every 6 minutes). Videos are available. See the following links 6b and 7b.

Also, while the collective migration example was inspired by the cancer biology literature [63, 73], Martinson et al. [77] produced a similar model. In this work, they model neural crest cell invasion, also using ECM remodeling cells that lead phenotypically similar, but non-remodeling cells. While varying in some aspects (such as using haptotaxis and only cell-cell repulsion), their use of a similar leader-follower model in developmental biology hints at this model's and the framework's applicability to more general leader-follower migration models.

4 Discussion

In this work, we presented a framework designed to capture salient aspects of bidirectional local cell-ECM interactions using a relatively simple mathematical model. Drawing on previous works, we developed a computational matrix using a mesh of voxels (ECM elements), each described by a limited set of features: overall anisotropy, overall directionality, and overall density. We added cell-ECM interactions including ECM-mediated changes in cellular motility (tunable contact guidance and ECM dependent cell migration speed) and cell-mediated local microstructure remodeling (changes to ECM element anisotropy, overall fiber orientation and density). Furthermore, through the use of PhysiCell rules [61], additional bidirectional interactions are possible without the need to write, compile, and test custom interaction code. We demonstrated the framework with three examples that focus on cell motility-ECM interactions: wound healing, basement membrane degradation, and collective migration. Each of these examples uses the same core framework with changes in source code only for simulation initialization. We make this newly implemented mesoscale, bidirectional cell-ECM interaction framework freely accessible to the community. With this powerful yet accessible framework, we aim to encourage and enable sharing of expertise among multiple problem domains (e.g., tumor biology, developmental biology, wound healing, angiogenesis, fibrosis). Furthermore, our approach opens up rich explorations of cell-matrix biology by allowing modelers to directly link a broad array of cell behaviors to ECM variables, without requiring additional coding on the part of modelers. This represents a key methodological advance in this work: enabling the exploration of a large set of relationships between cell behaviors and ECM state.

With this base framework constructed, it has the potential to continue to be extended. Here we discuss possible extensions. We note that our framework currently captures interactions between single ECM elements and single cells; it does not incorporate larger-scale interactions. This contrasts with other frameworks and models that represent the network like connections within a spatially-coupled ECM or distribute cellular remodeling and contact guidance among multiple ECM elements (e.g. - [24, 27, 55]). To address non-local remodeling of ECM, future efforts will focus on incorporating the option for a continuous, force-based ECM model, for example as a visco-poroelastic material using a finite element approach, then sampling the variables established in this work on the ECM element grid. To address the current limit of remodeling only a single ECM element, we aim to explore approaches to spread remodeling over multiple, adjacent ECM elements, for example with Gaussian smoothing or other techniques as well as enabling ECM influence on cell behavior from multiple ECM elements [55, 60]. Similarly, we aim to enable extending bidirectional cell-ECM interactions such that cells that span multiple elements can alter variables in each element it spans and be behaviorally influenced by them.

As noted in Section 2.2.2, due to ECM discretization, cells may miss ECM cues in regions of rapidly changing ECM orientation (high rates of path curvature) as observed in Figure 2b. ECM following is a function of cell speed, rates of curvature in an ECM path, and element size. To reduce the effect of the discretization, as needed, ECM element size can be decreased by users noting that decreasing element size will be balanced by decreasing the area of influence in the bidirectional cell-ECM interaction and will increase computational costs. The current default size of 20 μm per side was selected to be on the order of the size of the cell, as in a previous method [38]. This enables cells to modify a volume about equal to their volume, forming paths about one cell width in diameter (with our cell size of $\approx$ 17 μm. Future versions of the framework that include spreading the bidirectional cell-ECM influence over a region (discussed above) might ameliorate discretization effects by effectively smoothing the path.

In the initial version of the framework, we aimed to have simple constitutive relationships that produced a range of emergent behaviors. As an example, we model the anisotropy as only stable or increasing. This limits the ability to capture multiple, extensive remodelings of an ECM element. Future extensions to the framework could model both growth and decline in fiber-fiber alignment. Another possible extension is varying fiber following stochastically by sampling from a range of travel angles instead of deterministic contact guidance. Stochastic contact guidance was recently implemented using sampling from a von Mises distribution [60], showing its feasibility and interest within the community. Moreover, in future releases, we plan to generalize the framework architecture to enable users to easily replace built in constitutive relationships with their own relationships. Furthermore, architecture that allows easy exchange of one constitutive relationship for another would enable useful comparisons among model relationships. Future work could include comparing simulation outcomes, numerics, and computational performance of cell-ECM interaction formulations as similarly investigated for cell-cell constitutive relationships [78].

Finally, we note that the sample models were developed and are presented as a 2-D simulations (single slice of a 3-D environment), and could be, by reasonable extension of the cell-ECM interaction models to 3-D, be extended to 3-D. This extension to 3-D is additional future work for the framework.

5 Funding

We thank the Jayne Koskinas Ted Giovanis Foundation for Health and Policy and Breast Cancer Research Foundation for generous support. Additionally, this work was partially supported by the National Science Foundation (Grants 1735095 and 1720625).

6 Acknowledgements

We would like to thank Margherita Botecelli, Michael Getz, Adrianne Jenner, Heber Rocha, and Jordan Rozum for their expertise and assistance with this work. We gratefully acknowledge access to FutureSystems at the Digital Science Center, Luddy School of Informatics, Computing, and Engineering. This research was supported in part by Lilly Endowment, Inc., through its support for the Indiana University Pervasive Technology Institute.

References

[1] Frantz, C., Stewart, K.M., Weaver, V.M.: The extracellular matrix at a glance. Journal of Cell Science **123**(24), 4195–4200 (2010). https://doi.org/10.1242/jcs.023820

[2] Yue, B.: Biology of the Extracellular Matrix: An Overview. Journal of Glaucoma **23**, 20 (October/November 2014). https://doi.org/10.1097/IJG.0000000000000108

[3] Dzobo, K., Dandara, C.: The Extracellular Matrix: Its Composition, Function, Remodeling, and Role in Tumorigenesis. Biomimetics **8**(2), 146 (2023). https://doi.org/10.3390/biomimetics8020146

[4] Zaman, M.H., Trapani, L.M., Sieminski, A.L., MacKellar, D., Gong, H., Kamm, R.D., Wells, A., Lauffenburger, D.A., Matsudaira, P.: Migration of tumor cells in 3D matrices is governed by matrix stiffness along with cell-matrix adhesion and proteolysis. Proceedings of the National Academy of Sciences **103**(29), 10889–10894 (2006). https://doi.org/10.1073/pnas.0604460103

[5] Charras, G., Sahai, E.: Physical influences of the extracellular environment on cell migration. Nature Reviews Molecular Cell Biology **15**(12), 813–824 (2014). https://doi.org/10.1038/nrm3897

[6] Werb, Z., Sympson, C.J., Alexander, C.M., Thomasset, N., Lund, L.R., MacAuley, A., Ashkenas, J., Bissell, M.J.: Extracellular matrix remodeling and the regulation of epithelial-stromal interactions during differentiation and involution. Kidney international. Supplement **54**, 68–74 (1996)

[7] Ewald, A.J., Brenot, A., Duong, M., Chan, B.S., Werb, Z.: Collective Epithelial Migration and Cell Rearrangements Drive Mammary Branching Morphogenesis. Developmental Cell **14**(4), 570–581 (2008). https://doi.org/10.1016/j.devcel.2008.03.003

[8] Winkler, J., Abisoye-Ogunniyan, A., Metcalf, K.J., Werb, Z.: Concepts

of extracellular matrix remodelling in tumour progression and metastasis. Nature Communications **11**(1), 5120 (2020). https://doi.org/10.1038/s41467-020-18794-x

[9] Lu, P., Takai, K., Weaver, V.M., Werb, Z.: Extracellular Matrix Degradation and Remodeling in Development and Disease. Cold Spring Harbor Perspectives in Biology **3**(12), 005058–005058 (2011). https://doi.org/10.1101/cshperspect.a005058

[10] Cheung, K.J., Ewald, A.J.: Illuminating breast cancer invasion: Diverse roles for cell–cell interactions. Current Opinion in Cell Biology **30**, 99–111 (2014). https://doi.org/10.1016/j.ceb.2014.07.003

[11] Thrivikraman, G., Jagiełło, A., Lai, V.K., Johnson, S.L., Keating, M., Nelson, A., Schultz, B., Wang, C.M., Levine, A.J., Botvinick, E.L., Tranquillo, R.T.: Cell contact guidance via sensing anisotropy of network mechanical resistance. Proceedings of the National Academy of Sciences **118**(29), 2024942118 (2021). https://doi.org/10.1073/pnas.2024942118

[12] Carey, S.P., Goldblatt, Z.E., Martin, K.E., Romero, B., Williams, R.M., Reinhart-King, C.A.: Local extracellular matrix alignment directs cellular protrusion dynamics and migration through Rac1 and FAK. Integrative Biology **8**(8), 821–835 (2016). https://doi.org/10.1039/C6IB00030D

[13] Hastings, J.F., Skhinas, J.N., Fey, D., Croucher, D.R., Cox, T.R.: The extracellular matrix as a key regulator of intracellular signalling networks: ECM regulation of intracellular signalling networks. British Journal of Pharmacology **176**(1), 82–92 (2019). https://doi.org/10.1111/bph.14195

[14] Humphrey, J.D., Dufresne, E.R., Schwartz, M.A.: Mechanotransduction and extracellular matrix homeostasis. Nature Reviews Molecular Cell Biology **15**(12), 802–812 (2014). https://doi.org/10.1038/nrm3896

[15] Nguyen-Ngoc, K.-V., Cheung, K.J., Brenot, A., Shamir, E.R., Gray, R.S., Hines, W.C., Yaswen, P., Werb, Z., Ewald, A.J.: ECM microenvironment regulates collective migration and local dissemination in normal and malignant mammary epithelium. Proceedings of the National Academy of Sciences **109**(39), 2595–2604 (2012). https://doi.org/10.1073/pnas.1212834109

[16] Wynn, T.A., Vannella, K.M.: Macrophages in Tissue Repair, Regeneration, and Fibrosis. Immunity **44**(3), 450–462 (2016). https://doi.org/10.1016/j.immuni.2016.02.015

[17] Metzcar, J., Wang, Y., Heiland, R., Macklin, P.: A Review of Cell-Based Computational Modeling in Cancer Biology. JCO Clinical Cancer Informatics (3), 1–13 (2019). https://doi.org/10.1200/CCI.18.00069

[18] Jorgensen, S.N., Sanders, J.R.: Mathematical models of wound healing and closure: A comprehensive review. Medical & Biological Engineering & Computing **54**(9), 1297–1316 (2016). https://doi.org/10.1007/s11517-015-1435-z

[19] Leonard-Duke, J., Evans, S., Hannan, R.T., Barker, T.H., Bates, J.H.T., Bonham, C.A., Moore, B.B., Kirschner, D.E., Peirce, S.M.: Multi-scale models of lung fibrosis. Matrix Biology **91–92**, 35–50 (2020). https://doi.org/10.1016/j.matbio.2020.04.003

[20] Crossley, R.M., Johnson, S., Tsingos, E., Bell, Z., Berardi, M., Botticelli, M., Braat, Q.J.S., Metzcar, J., Ruscone, M., Yin, Y., Shuttleworth, R.: Demystifying the Extracellular Matrix: A Review of Current Mathematical Approaches and Recent Perspectives. arXiv (2023). https://doi.org/10.48550/arXiv.2312.12365

[21] Schlüter, D.K., Ramis-Conde, I., Chaplain, M.A.J.: Computational Modeling of Single-Cell Migration: The Leading Role of Extracellular Matrix Fibers. Biophysical Journal **103**(6), 1141–1151 (2012). https://doi.org/10.1016/j.bpj.2012.07.048

[22] Noel, V., Ruscone, M., Shuttleworth, R., MacNamara, C.K.: PhysiMeSS - A New PhysiCell Addon for Extracellular Matrix Modelling. bioRxiv (2023). https://doi.org/10.1101/2023.10.27.564365

[23] Macnamara, C.K., Caiazzo, A., Ramis-Conde, I., Chaplain, M.A.J.: Computational modelling and simulation of cancer growth and migration within a 3D heterogeneous tissue: The effects of fibre and vascular structure. Journal of Computational Science **40**, 101067 (2020). https://doi.org/10.1016/j.jocs.2019.101067

[24] Zhu, J., Mogilner, A.: Comparison of cell migration mechanical strategies in three-dimensional matrices: A computational study. Interface focus **6**(5), 20160040 (2016). https://doi.org/10.1098/rsfs.2016.0040

[25] Tozluoğlu, M., Tournier, A.L., Jenkins, R.P., Hooper, S., Bates, P.A., Sahai, E.: Matrix geometry determines optimal cancer cell migration strategy and modulates response to interventions. Nature Cell Biology **15**(7), 751–762 (2013). https://doi.org/10.1038/ncb2775

[26] Tsingos, E., Bakker, B.H., Keijzer, K.A.E., Hupkes, H.J., Merks, R.M.H.: Modelling the Mechanical Cross-Talk between Cells and Fibrous Extracellular Matrix Using Hybrid Cellular Potts and Molecular Dynamics Methods. bioRxiv (2022). https://doi.org/10.1101/2022.06.10.495667

[27] van Oers, R.F.M., Rens, E.G., LaValley, D.J., Reinhart-King, C.A., Merks, R.M.H.: Mechanical Cell-Matrix Feedback Explains Pairwise and

Collective Endothelial Cell Behavior In Vitro. PLOS Computational Biology **10**(8), 1003774 (2014). https://doi.org/10.1371/journal.pcbi.1003774

[28] Ahmadzadeh, H., Webster, M.R., Behera, R., Jimenez Valencia, A.M., Wirtz, D., Weeraratna, A.T., Shenoy, V.B.: Modeling the two-way feedback between contractility and matrix realignment reveals a nonlinear mode of cancer cell invasion. Proceedings of the National Academy of Sciences **114**(9), 1617–1626 (2017). https://doi.org/10.1073/pnas.1617037114

[29] Anderson, A.: Continuous and Discrete Mathematical Models of Tumor-induced Angiogenesis. Bulletin of Mathematical Biology **60**(5), 857–899 (1998). https://doi.org/10.1006/bulm.1998.0042

[30] Zeng, W., Thomas, G.L., Glazier, J.A.: Non-Turing stripes and spots: A novel mechanism for biological cell clustering. Physica A: Statistical Mechanics and its Applications **341**, 482–494 (2004). https://doi.org/10.1016/j.physa.2004.03.089

[31] Daub, J.T., Merks, R.M.H.: A Cell-Based Model of Extracellular-Matrix-Guided Endothelial Cell Migration During Angiogenesis. Bulletin of Mathematical Biology **75**(8), 1377–1399 (2013). https://doi.org/10.1007/s11538-013-9826-5

[32] Trucu, D., Lin, P., Chaplain, M.A.J., Wang, Y.: A Multiscale Moving Boundary Model Arising in Cancer Invasion. Multiscale Modeling & Simulation **11**(1), 309–335 (2013). https://doi.org/10.1137/110839011

[33] Shuttleworth, R., Trucu, D.: Multiscale Modelling of Fibres Dynamics and Cell Adhesion within Moving Boundary Cancer Invasion. Bulletin of Mathematical Biology **81**(7), 2176–2219 (2019). https://doi.org/10.1007/s11538-019-00598-w

[34] Shuttleworth, R., Trucu, D.: Cell-Scale Degradation of Peritumoural Extracellular Matrix Fibre Network and Its Role Within Tissue-Scale Cancer Invasion. Bulletin of Mathematical Biology **82**(6), 65 (2020). https://doi.org/10.1007/s11538-020-00732-z

[35] Gonçalves, I.G., Garcia-Aznar, J.M.: Extracellular matrix density regulates the formation of tumour spheroids through cell migration. PLOS Computational Biology **17**(2), 1–22 (2021). https://doi.org/10.1371/journal.pcbi.1008764

[36] Letort, G., Montagud, A., Stoll, G., Heiland, R., Barillot, E., Macklin, P., Zinovyev, A., Calzone, L.: PhysiBoSS: A multi-scale agent-based modelling framework integrating physical dimension and cell signalling. Bioinformatics **35**(7), 1188–1196 (2019). https://doi.org/10.1093/

bioinformatics/bty766

[37] Ponce-de-Leon, M., Montagud, A., Noël, V., Meert, A., Pradas, G., Barillot, E., Calzone, L., Valencia, A.: PhysiBoSS 2.0: A sustainable integration of stochastic Boolean and agent-based modelling frameworks. npj Systems Biology and Applications **9**(1), 1–12 (2023). https://doi.org/10.1038/s41540-023-00314-4

[38] Ghaffarizadeh, A., Heiland, R., Friedman, S.H., Mumenthaler, S.M., Macklin, P.: PhysiCell: An open source physics-based cell simulator for 3-D multicellular systems. PLOS Computational Biology **14**(2), 1005991 (2018). https://doi.org/10.1371/journal.pcbi.1005991

[39] Stoll, G., Caron, B., Viara, E., Dugourd, A., Zinovyev, A., Naldi, A., Kroemer, G., Barillot, E., Calzone, L.: MaBoSS 2.0: An environment for stochastic Boolean modeling. Bioinformatics **33**(14), 2226–2228 (2017). https://doi.org/10.1093/bioinformatics/btx123

[40] Ruscone, M., Montagud, A., Chavrier, P., Destaing, O., Bonnet, I., Zinovyev, A., Barillot, E., Noël, V., Calzone, L.: Multiscale model of the different modes of cancer cell invasion. Bioinformatics **39**(6), 374 (2023). https://doi.org/10.1093/bioinformatics/btad374

[41] Chauviere, A., Hillen, T., Preziosi, L.: Modeling cell movement in anisotropic and heterogeneous network tissues. Networks & Heterogeneous Media **2**(2), 333–357 (2007). https://doi.org/10.3934/nhm.2007.2.333

[42] Hillen, T.: M5 mesoscopic and macroscopic models for mesenchymal motion. Journal of Mathematical Biology **53**(4), 585–616 (2006). https://doi.org/10.1007/s00285-006-0017-y

[43] Painter, K.J.: Modelling cell migration strategies in the extracellular matrix. Journal of Mathematical Biology **58**(4), 511–543 (2009). https://doi.org/10.1007/s00285-008-0217-8

[44] Graner, F., Glazier, J.A.: Simulation of biological cell sorting using a two-dimensional extended Potts model. Physical Review Letters **69**(13), 2013–2016 (1992). https://doi.org/10.1103/PhysRevLett.69.2013

[45] Bauer, A.L., Jackson, T.L., Jiang, Y.: A Cell-Based Model Exhibiting Branching and Anastomosis during Tumor-Induced Angiogenesis. Biophysical Journal **92**(9), 3105–3121 (2007). https://doi.org/10.1529/biophysj.106.101501

[46] Rubenstein, B.M., Kaufman, L.J.: The Role of Extracellular Matrix in Glioma Invasion: A Cellular Potts Model Approach. Biophysical Journal

95, 5661–5680 (2008). https://doi.org/10.1529/biophysj.108.140624

[47] Scianna, M., Preziosi, L., Wolf, K.: A Cellular Potts model simulating cell migration on and in matrix environments. Mathematical Biosciences and Engineering **10**(1), 235–261 (2013). https://doi.org/10.3934/mbe.2013.10.235

[48] Szabó, A., Varga, K., Garay, T., Hegedűs, B., Czirók, A.: Invasion from a cell aggregate—the roles of active cell motion and mechanical equilibrium. Physical Biology **9**(1), 016010 (2012). https://doi.org/10.1088/1478-3975/9/1/016010

[49] Kumar, S., Kapoor, A., Desai, S., Inamdar, M.M., Sen, S.: Proteolytic and non-proteolytic regulation of collective cell invasion: Tuning by ECM density and organization. Scientific Reports **6**(1), 19905 (2016). https://doi.org/10.1038/srep19905

[50] Vicsek, T., Czirok, A., Ben-Jacob, E., Cohen, I., Shochet, O.: Novel Type of Phase Transition in a System of Self-Driven Particles. Physical Review Letters **75**(6), 1226–1229 (1995). https://doi.org/10.1103/PhysRevLett.75.1226

[51] Park, D., Wershof, E., Boeing, S., Labernadie, A., Jenkins, R.P., George, S., Trepat, X., Bates, P.A., Sahai, E.: Extracellular matrix anisotropy is determined by TFAP2C-dependent regulation of cell collisions. Nature Materials **19**(2), 227–238 (2020). https://doi.org/10.1038/s41563-019-0504-3

[52] Suveges, S., Chamseddine, I., Rejniak, K.A., Eftimie, R., Trucu, D.: Collective Cell Migration in a Fibrous Environment: A Hybrid Multiscale Modelling Approach. Frontiers in Applied Mathematics and Statistics **7** (2021)

[53] Olsen, L., Maini, P.K., Sherratt, J.A., Dallon, J.: Mathematical modelling of anisotropy in fibrous connective tissue. Mathematical Biosciences **158**(2), 145–170 (1999). https://doi.org/10.1016/S0025-5564(99)00005-X

[54] Dallon, J.C., Sherratt, J.A.: A Mathematical Model for Spatially Varying Extracellular Matrix Alignment. SIAM Journal on Applied Mathematics **61**(2), 506–527 (2000). https://doi.org/10.1137/S0036139999359343

[55] Dallon, J.C., Sherratt, J.A., Maini, P.K.: Mathematical Modelling of Extracellular Matrix Dynamics using Discrete Cells: Fiber Orientation and Tissue Regeneration. Journal of Theoretical Biology **199**(4), 449–471 (1999). https://doi.org/10.1006/jtbi.1999.0971

[56] Dallon, J., Sherratt, J., Maini, P., Ferguson, M.: Biological implications of a discrete mathematical model for collagen deposition and alignment in dermal wound repair. Mathematical Medicine and Biology: A Journal of the IMA **17**(4), 379–393 (2000). https://doi.org/10.1093/imammb/17.4.379

[57] Dallon, J.C., Sherratt, J.A., Maini, P.K.: Modeling the effects of transforming growth factor-β on extracellular matrix alignment in dermal wound repair. Wound Repair and Regeneration **9**(4), 278–286 (2001). https://doi.org/10.1046/j.1524-475X.2001.00278.x

[58] Sherratt, J.A., Dallon, J.C.: Theoretical models of wound healing: Past successes and future challenges. Comptes Rendus Biologies **325**(5), 557–564 (2002). https://doi.org/10.1016/S1631-0691(02)01464-6

[59] McDougall, S., Dallon, J., Sherratt, J., Maini, P.: Fibroblast migration and collagen deposition during dermal wound healing: Mathematical modelling and clinical implications. Philosophical Transactions of the Royal Society A: Mathematical, Physical and Engineering Sciences **364**(1843), 1385–1405 (2006). https://doi.org/10.1098/rsta.2006.1773

[60] Martinson, W.D., McLennan, R., Teddy, J.M., McKinney, M.C., Davidson, L.A., Baker, R.E., Byrne, H.M., Kulesa, P.M., Maini, P.K.: Dynamic fibronectin assembly and remodeling by leader neural crest cells prevents jamming in collective cell migration. eLife **12**, 83792 (2023). https://doi.org/10.7554/eLife.83792

[61] Johnson, J.A.I., Stein-O'Brien, G.L., Booth, M., Heiland, R., Kurtoglu, F., Bergman, D.R., Bucher, E., Deshpande, A., Forjaz, A., Getz, M., Godet, I., Lyman, M., Metzcar, J., Mitchell, J., Raddatz, A., Rocha, H., Solorzano, J., Sundus, A., Wang, Y., Gilkes, D., Kagohara, L.T., Kiemen, A.L., Thompson, E.D., Wirtz, D., Wu, P.-H., Zaidi, N., Zheng, L., Zimmerman, J.W., Jaffee, E.M., Chang, Y.H., Coussens, L.M., Gray, J.W., Heiser, L.M., Fertig, E.J., Macklin, P.: Digitize Your Biology! Modeling Multicellular Systems through Interpretable Cell Behavior. bioRxiv (2023). https://doi.org/10.1101/2023.09.17.557982

[62] Ghaffarizadeh, A., Friedman, S.H., Macklin, P.: BioFVM: An efficient, parallelized diffusive transport solver for 3-D biological simulations. Bioinformatics **32**(8), 1256–1258 (2016). https://doi.org/10.1093/bioinformatics/btv730

[63] Cheung, K.J., Gabrielson, E., Werb, Z., Ewald, A.J.: Collective Invasion in Breast Cancer Requires a Conserved Basal Epithelial Program. Cell **155**(7), 1639–1651 (2013). https://doi.org/10.1016/j.cell.2013.11.029

[64] Duggan, B., Metzcar, J., Macklin, P.: DAPT: A package enabling distributed automated parameter testing. Gigabyte **2021**, 1–10 (2021). https://doi.org/10.46471/gigabyte.22

[65] Heiland, R., Mishler, D., Zhang, T., Bower, E., Macklin, P.: Xml2jupyter: Mapping parameters between XML and Jupyter widgets. Journal of Open Source Software **4**(39), 1408 (2019). https://doi.org/10.21105/joss.01408

[66] Gurtner, G.C., Werner, S., Barrandon, Y., Longaker, M.T.: Wound repair and regeneration. Nature **453**(7193), 314–321 (2008). https://doi.org/10.1038/nature07039

[67] Betensley, A., Sharif, R., Karamichos, D.: A Systematic Review of the Role of Dysfunctional Wound Healing in the Pathogenesis and Treatment of Idiopathic Pulmonary Fibrosis. Journal of Clinical Medicine **6**(1), 2 (2017). https://doi.org/10.3390/jcm6010002

[68] Cumming, B.D., McElwain, D.L.S., Upton, Z.: A mathematical model of wound healing and subsequent scarring. Journal of The Royal Society Interface **7**(42), 19–34 (2009). https://doi.org/10.1098/rsif.2008.0536

[69] Chang, J., Chaudhuri, O.: Beyond proteases: Basement membrane mechanics and cancer invasion. Journal of Cell Biology **218**(8), 2456–2469 (2019). https://doi.org/10.1083/jcb.201903066

[70] Strell, C., Paulsson, J., Jin, S.-B., Tobin, N.P., Mezheyeuski, A., Roswall, P., Mutgan, C., Mitsios, N., Johansson, H., Wickberg, S.M., Svedlund, J., Nilsson, M., Hall, P., Mulder, J., Radisky, D.C., Pietras, K., Bergh, J., Lendahl, U., Wärnberg, F., Östman, A.: Impact of Epithelial–Stromal Interactions on Peritumoral Fibroblasts in Ductal Carcinoma in Situ. JNCI: Journal of the National Cancer Institute **111**(9), 983–995 (2019). https://doi.org/10.1093/jnci/djy234

[71] Kim, Y., Othmer, H.G.: A Hybrid Model of Tumor–Stromal Interactions in Breast Cancer. Bulletin of Mathematical Biology **75**(8), 1304–1350 (2013). https://doi.org/10.1007/s11538-012-9787-0

[72] Brown, P.J., Green, J.E.F., Binder, B.J., Osborne, J.M.: A rigid body framework for multicellular modeling. Nature Computational Science **1**(11), 754–766 (2021). https://doi.org/10.1038/s43588-021-00154-4

[73] Carey, S.P., Starchenko, A., McGregor, A.L., Reinhart-King, C.A.: Leading malignant cells initiate collective epithelial cell invasion in a three-dimensional heterotypic tumor spheroid model. Clinical & Experimental Metastasis **30**(5), 615–630 (2013). https://doi.org/10.1007/s10585-013-9565-x

[74] Ozik, J., Collier, N., Heiland, R., An, G., Macklin, P.: Learning-accelerated Discovery of Immune-Tumour Interactions. Preprint, Systems Biology (March 2019). https://doi.org/10.1101/573972

[75] Ilina, O., Gritsenko, P.G., Syga, S., Lippoldt, J., La Porta, C.A.M., Chepizhko, O., Grosser, S., Vullings, M., Bakker, G.-J., Starruß, J., Bult, P., Zapperi, S., Käs, J.A., Deutsch, A., Friedl, P.: Cell–cell adhesion and 3D matrix confinement determine jamming transitions in breast cancer invasion. Nature Cell Biology **22**(9), 1103–1115 (2020). https://doi.org/10.1038/s41556-020-0552-6

[76] Kang, W., Ferruzzi, J., Spatarelu, C.-P., Han, Y.L., Sharma, Y., Koehler, S.A., Mitchel, J.A., Khan, A., Butler, J.P., Roblyer, D., Zaman, M.H., Park, J.-A., Guo, M., Chen, Z., Pegoraro, A.F., Fredberg, J.J.: A novel jamming phase diagram links tumor invasion to non-equilibrium phase separation. iScience **24**(11), 103252 (2021). https://doi.org/10.1016/j.isci.2021.103252

[77] Martinson, W.D., McLennan, R., Teddy, J.M., McKinney, M.C., Davidson, L.A., Baker, R.E., Byrne, H.M., Kulesa, P.M., Maini, P.K.: Dynamic Fibronectin Assembly and Remodeling by Leader Neural Crest Cells Prevents Jamming in Collective Cell Migration. arXiv (2022). https://doi.org/10.48550/arXiv.2209.07794

[78] Mathias, S., Coulier, A., Bouchnita, A., Hellander, A.: Impact of Force Function Formulations on the Numerical Simulation of Centre-Based Models. Bulletin of Mathematical Biology **82**(10), 132 (2020). https://doi.org/10.1007/s11538-020-00810-2

[79] Macklin, P., Edgerton, M.E., Thompson, A.M., Cristini, V.: Patient-calibrated agent-based modelling of ductal carcinoma in situ (DCIS): From microscopic measurements to macroscopic predictions of clinical progression. Journal of Theoretical Biology **301**, 122–140 (2012). https://doi.org/10.1016/j.jtbi.2012.02.002

[80] D'Antonio, G., Macklin, P., Preziosi, L., D'Antonio, G., Macklin, P., Preziosi, L.: An agent-based model for elasto-plastic mechanical interactions between cells, basement membrane and extracellular matrix. Mathematical Biosciences and Engineering **10**(1), 75–101 (2013). https://doi.org/10.3934/mbe.2013.10.75

[81] Drasdo, D., Kree, R., McCaskill, J.S.: Monte Carlo approach to tissue-cell populations. Physical Review E **52**(6), 6635–6657 (1995). https://doi.org/10.1103/PhysRevE.52.6635

[82] Galle, J., Loeffler, M., Drasdo, D.: Modeling the Effect of Deregulated Proliferation and Apoptosis on the Growth Dynamics of Epithelial Cell

Populations In Vitro. Biophysical Journal **88**(1), 62–75 (2005). https://doi.org/10.1529/biophysj.104.041459

[83] Johnson, J.A.I., Stein-O'Brien, G.L., Booth, M., Heiland, R., Kurtoglu, F., Bergman, D.R., Bucher, E., Deshpande, A., Forjaz, A., Getz, M., Godet, I., Lyman, M., Metzcar, J., Mitchell, J., Raddatz, A., Rocha, H., Solorzano, J., Sundus, A., Wang, Y., Gilkes, D., Kagohara, L.T., Kiemen, A.L., Thompson, E.D., Wirtz, D., Wu, P.-H., Zaidi, N., Zheng, L., Zimmerman, J.W., Jaffee, E.M., Chang, Y.H., Coussens, L.M., Gray, J.W., Heiser, L.M., Fertig, E.J., Macklin, P.: Digitize Your Biology! Modeling Multicellular Systems through Interpretable Cell Behavior. bioRxiv (2023). https://doi.org/10.1101/2023.09.17.557982

[84] Grote, J., Süsskind, R., Vaupel, P.: Oxygen diffusivity in tumor tissue (DS-Carcinosarcoma) under temperature conditions within the range of 20–40°C. Pflügers Archiv **372**(1), 37–42 (1977). https://doi.org/10.1007/BF00582204

[85] McKeown, S.R.: Defining normoxia, physoxia and hypoxia in tumours—implications for treatment response. The British Journal of Radiology **87**(1035), 20130676 (2014). https://doi.org/10.1259/bjr.20130676

7 Supplementary Material

7.1 Cell remodeling of ECM microstructure

Here we detail the mathematical models for updating ECM anisotropy, orientation, and density - the methods of writing a signal to the matrix or otherwise remodeling it. The ECM elements and cells are conceived of as being in close contact; cells alter the ECM element they are physically in. To formalize which ECM element a cell modifies out of the many possible options (see Figure 1a), we define cells as interacting with whichever element their center coordinates are the closest to, as in [38]. To do this, suppose cell i is at position $\mathbf{x}_i$. We remodel the ECM element whose center $\mathbf{x}_i^*$ is closest to $\mathbf{x}_i$t. We outline two related methods for writing signals and altering ECM microstructure - the limit case of instantaneous signal writing and the non-instantaneous case.

Instant anisotropy and orientation remodeling

To explore an extreme case of ECM mediated communication, we model anisotropy and ECM element orientation as being immediately updated when contacted by a remodeling cell, resulting in the following relationships to update a and $\mathbf{f}$:

$$a(\mathbf{x}_i^*) = 1 \tag{1}$$

$$\mathbf{f}(\mathbf{x}_i^*) = \mathbf{d}_{\mathbf{remodeler}}. \tag{2}$$

Because of the underlying updates to $\mathbf{f}$ (see next subsection), this permanently writes with high signal strength the motility direction of the first cell to pass through a particular ECM element.

Non-instantaneous microstructure remodeling

Anisotropy

Anisotropy is represented by a scalar ranging from 0 to 1, representing "complete lack of anisotropy" (or a disordered state) to "complete anisotropy" (a highly ordered state). The rate of change in anisotropy over time is given as:

$$\frac{da(\mathbf{x}_i^*)}{dt} = r_a(1 - a(\mathbf{x}_i^*)). \tag{3}$$

r_a is specified as:

$$r_a = r_{a_0} s_{\text{cell}} \tag{4}$$

where r_{a0} is a base rate of change and s_{cell} is the migration speed of the cell changing the ECM element's anisotropy.

Orientation

We model changes to fiber orientation as follows:

$$\frac{d\mathbf{f}(\mathbf{x}_i^*)}{dt} = -r_f \left(\mathbf{f}(\mathbf{x}_i^*) - \frac{\mathbf{d_{remodeler}}}{||\mathbf{d_{remodeler}}||} \right) \tag{5}$$

with

$$r_f = r_{f_0} s_{\text{cell}}(1-a). \tag{6}$$

r_{f_0} is the base rate of change, $\mathbf{d_{remodeler}}$ is the direction of the remodeling cell, and s_{cell} is cell speed. $\boldsymbol{f}$ is normalized after each update. Note that when $a = 1$, orientation cannot change. Also, we select to remodel $\mathbf{f}$ such that it takes on the smallest angle between it and $\mathbf{d_{remodeler}}$.

Density

Density ranges from 0 to 1, representing a fluid-filled region to a very dense region completely filled with ECM material, respectively. Cells change ECM density locally through the following relationship:

$$\frac{d\rho(\mathbf{x}_i^*)}{dt} = r_{density}(\rho_{target} - \rho(\mathbf{x}_i^*)) \tag{7}$$

where $r_{density}$ is the cell's characteristic rate of deposition/degradation of ECM and ρ_{target} is the cell's target for ECM density.

7.2 ECM microstructure influence on cell motility

Cell motion, in particular, cell speed and direction, can be altered via cell-ECM interactions. ECM element orientation and anisotropy are combined with a cell's preferred direction to produce the cell motility vector. Independently, cell speed is influenced by ECM density enabling ECM to block or guide cell paths. We layout the orientation and anisotropy influences first, then the influence of density. As with writing signals to the ECM, we define cells to be in and read whichever element their center coordinates are the closest to, as in [38].

7.2.1 ECM orientation and anisotropy

We developed a method to calculate $\mathbf{d_{actual}}$, a cell's actual motility direction, based on the cell's preferred direction $\mathbf{d_{preferred}}$, a cell specific ECM sensitivity s, and local anisotropy and orientation. As illustrated in Supplementary Figure 1, we want to constrain cell motion to the sector spanning the ECM orientation ($\mathbf{f}$) and the cell's intended direction of travel ($\mathbf{d_{preferred}}$) in a way that does not bias direction of travel along the fibers. We use $\mathbf{f}$ and $\mathbf{d_{preferred}}$ to form an orthonormal basis set that spans the cell's potential directions (the sector produced by the angle θ in Figure 1d). We calculate $\mathbf{d_{actual}}$ by blending the basis vectors using the cell's ECM sensitivity parameter s and local ECM element's anisotropy a as follows:

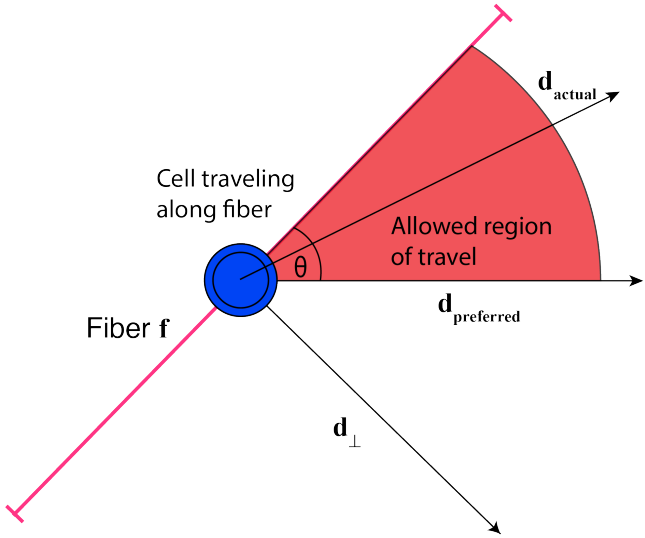

Supplementary Figure 1: Schematic for mathematical model of cell motility and ECM orientation interactions. Cell shown in blue. See 8, 10, and 12 for variable explanations.

$$\mathbf{d_{actual}} = (1-\gamma)C_1\mathbf{d}_\perp + C_2\mathbf{f}, \tag{8}$$

where γ is the effective ECM influence parameter. This captures both cell sensitivity and magnitude of ECM fiber alignment (signal strength):

$$\gamma = a(\mathbf{x_i}) \cdot s_i. \tag{9}$$

s_i and $a(\mathbf{x}_i^*)$ are the sensitivity of cell i and anisotropy at that location respectively. The other terms in Equation 8, the coefficients C_1 and C_2 and basis vector $\mathbf{d}_\perp$, are calculated by decomposing $\mathbf{d_{preferred}}$ and basic trigonometry. For brevity, we will drop location and indexing of cells unless needed for clarity.

We find $\mathbf{d}_\perp$, using the trigonometric relationship $\mathbf{A} \cdot \mathbf{B} = ||\mathbf{A}||||\mathbf{B}||\cos\,\theta$. Letting $\mathbf{f}$ and $\mathbf{d_{preferred}}$ be unit vectors and θ being the angle between them, the relationship simplifies to:

$$\mathbf{d_{preferred}} \cdot \mathbf{f} = \cos\,\theta. \tag{10}$$

Scaling $\mathbf{f}$ by that dot product, we get the component of $\mathbf{d_{preferred}}$ that points along $\mathbf{f}$. Subtracting that result from $\mathbf{d_{preferred}}$, we obtain a vector perpendicular to $\mathbf{f}$ as follows:

$$\mathbf{d}_\perp^{'} = \mathbf{d_{preferred}} - (\mathbf{d_{preferred}} \cdot \mathbf{f})\mathbf{f} \tag{11}$$

with normalization producing the unit vector $\mathbf{d}_\perp$ seen in Equation 8 and Figure 1d.

Note also that $\mathbf{d_{preferred}}$ can be decomposed as follows:

$$\mathbf{d_{preferred}} = C_1\mathbf{d}_\perp + C_2\mathbf{f} \tag{12}$$

with C_1 and C_2 the same as in Equation 8. They are determined via dot product and again, we take advantage of the terms being unit vectors:

$$\begin{aligned}\mathbf{d_{preferred}} \cdot \mathbf{d}_\perp &= (C_1\mathbf{d}_\perp + C_2\mathbf{f}) \cdot \mathbf{d}_\perp \\ &= C_1\mathbf{d}_\perp \cdot \mathbf{d}_\perp + C_2\mathbf{f} \cdot \mathbf{d}_\perp \\ &= C_1. \end{aligned} \tag{13}$$

Likewise, by dotting both sides of Equation 12 by $\mathbf{f}$, we obtain C_2 as follows:

$$\begin{aligned}\mathbf{d_{preferred}} \cdot \mathbf{f} &= (C_1\mathbf{d}_\perp + C_2\mathbf{f}) \cdot \mathbf{f} \\ &= C_1\mathbf{d}_\perp \cdot \mathbf{f} + C_2\mathbf{f} \cdot \mathbf{f} \\ &= C_2. \end{aligned} \tag{14}$$

With that, all required parts of Equation 8 are determined, letting $\mathbf{d_{actual}}$ be calculated. Note that if the effective influence parameter γ is zero, Equation 8 becomes Equation 12, meaning $\mathbf{d_{actual}}$ will equal $\mathbf{d_{preferred}}$. Likewise, when γ is one, its maximum value, $\mathbf{d_{actual}}$ equals $\mathbf{f}$.

In the case that $\mathbf{d_{preferred}}$ is parallel to $\mathbf{f}$, $\mathbf{d}_\perp^{'}$ from Equation 11 is the zero vector. We assume the norm of the zero vector to be zero. With that set, the calculations will proceed as normal.

Note that there are two possibilities on how to interpret $\mathbf{d_{actual}}$:

A: The cell senses its environment, determines direction of travel along the fibers, and all cell effort goes into that motion.

B: The cell attempts to move both along the fibers and along its preferred direction, wasting effort in the process.

These two interpretations lead to either normalizing $\mathbf{d_{actual}}$ (Option **A**) or letting the cell direction vector lose magnitude by not normalizing $\mathbf{d_{actual}}$ (Option **B**). For the purposes of this work, we choose Option **B** and do not normalize $\mathbf{d_{actual}}$.

Constitutive relations to determine $\mathbf{d_{preferred}}$

To determine $\mathbf{d_{preferred}}$ in Equation 8, we extend the motility model of [38]'s motility model.

Model I: Chemotaxis based motility

To determine $\mathbf{d_{preferred}}$ for chemotactically motivated cells, we use the following equation from [38]:

$$\mathbf{d_{preferred}} = (1 - b) \cdot \mathbf{d_{random}} + b \cdot \mathbf{d_{chemotaxis}} \tag{15}$$

where $\mathbf{d_{random}}$ is a randomly generated unit vector, $\mathbf{d_{chemotaxis}}$ is a unit length microenvironment-derived direction, such as the gradient of a cell-required substrate, and the scalar b, running from 0 - 1, is the directional bias parameter that sets the balance between random (b=0) and completely biased cell motility r, (b=1). $\mathbf{d_{preferred}}$ is the cell-selected motility direction and may be combined with local fiber orientation to produce the final cell motility direction.

Model II: ECM and chemotaxis based motility

To couple chemotactic behavior with reading of ECM signals, we reformulated Equation 15 and replace the chemotactic bias with the local ECM anisotropy:

$$\mathbf{d_{preferred}} = (1-a)\cdot\mathbf{d_{random}} + a\cdot\mathbf{d_{chemotaxis}} \tag{16}$$

Here, a replaces the bias parameter in setting the random versus chemotactic behavior. When combined with the cell-ECM interactions, this model effectively enables a cell to only be chemotactic when in an element of anisotropic ECM.

7.2.2 ECM density

We use the following relationship to incorporate the influence of ECM density ρ on cell speed:

$$s_{\text{cell}} = \begin{cases} 0 & \text{if } \rho \leq \rho_l \\ S_{max}\frac{\rho-\rho_l}{\rho_{ideal}-\rho_l} & \text{if } \rho_l < \rho \leq \rho_{ideal} \\ S_{max}\frac{\rho-\rho_h}{\rho_{ideal}-\rho_h} & \text{if } \rho_{ideal} < \rho < \rho_h \\ 0 & \text{if } \rho \geq \rho_h \end{cases} \tag{17}$$

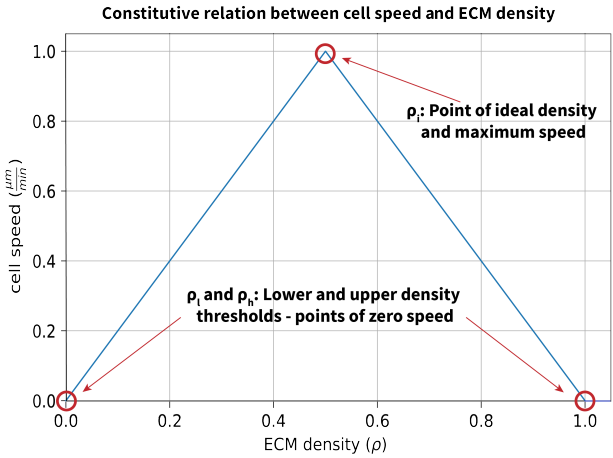

Supplementary Figure 2: Constitutive relationship between cell speed and density. This is the graphical form of Equation 7.2.2 with parameters used for the example models.

where ρ is the local ECM density, S_{max} is the maximum cell migration speed, ρ_l is the ECM threshold density above which cells have non-zero speed, ρ_h is

the ECM threshold density above which cells cannot move, and ρ_{ideal} is the ECM density of maximum speed. Supplementary Figure 2 shows the tent-like shape of Equation 7.2.2 with the parameters used in our example models.

This form simulates a cell that in an fibrous environment cannot move either when density is too low, due to a lack of fibers to grab onto for propulsion, or when density is too high, meaning the ECM is too dense for the cell to pass through. Other polynomials or curves derived from fitting to data could be used in place of this form. We choose it to be a minimum example of a tunable, potentially asymmetric curve with a local maximum.

7.3 Cell velocity and cell-cell adhesion and repulsion model

In PhysiCell, the ABM framework our examples and ECM model are built in, cell velocities and positions update based on several forces - cell-cell forces as well as cell-environmental forces and cell-locomotive force. In this current work, we focused on cell-cell forces (cell-adhesion and repulsion) as well as cell locomotive forces. The locomotive force is covered in the previous section including chemotaxis and impacts of ECM on cell motility. To discuss cell-cell adhesion and repulsion, we follow the explanation from [38], beginning with the cell equation of motion. See [38] and [79] for additional details and discussion.

Given a cell i at position $\mathbf{x}_i(t)$, velocity $\mathbf{v}_i(t)$ and a set of neighboring cells $\mathcal{N}(i)$, PhysiCell models cell motion with this equation:

$$m_i \dot{\mathbf{v}}_i = \sum_{j \in \mathcal{N}} (\mathbf{F}^{ij}_{\text{cca}} + \mathbf{F}^{ij}_{\text{ccr}}) + \mathbf{F}^{i}_{\text{drag}} + \mathbf{F}^{i}_{\text{loc}} \tag{18}$$

where $\mathbf{F}_{\text{cca}}$ and $\mathbf{F}_{\text{ccr}}$ are the cell-cell adhesive and repulsive (cell resistance to deformation) forces, $\mathbf{F}_{\text{drag}}$ represents dissipative, drag-like forces such as viscous drag, and $\mathbf{F}_{\text{loc}}$ is cell generated, or motile, force. Note that as appropriate, additional forces can be added to this term, such as cell-basement membrane adhesion and repulsion (see [38] and [79]).

Examining this term by term, drag is modeled as follows [38, 79, 80]:

$$\mathbf{F}_{\text{drag}} = \nu \mathbf{v}_i. \tag{19}$$

Here, ν is a drag coefficient. This differs from the formulation in [38], which also included a drag term for ECM interactions. Since we model ECM interactions explicitly in the update for cell locomotive force, we do not it include it here. The formulation makes the inertialess assumption ($m_i \dot{\mathbf{v}}_i \approx 0$) [38, 79, 81, 82] which assumes that forces equilibrate quickly. Making these substitutions in Equation 18 and solving for $\mathbf{v}_i$, we get:

$$\mathbf{v}_i = \frac{1}{\nu}\left(\sum_{j\in\mathcal{N}}(\mathbf{F}^{ij}_{\text{cca}} + \mathbf{F}^{ij}_{\text{ccr}}) + \mathbf{F}^{i}_{\text{loc}}\right). \tag{20}$$

As noted in [79], this assumption yields the interpretation of each term as the terminal velocity of the cell, given that only the force of interest and drag are acting on the cell. The $\mathbf{F}_{\text{cca}}$ and $\mathbf{F}_{\text{ccr}}$ are then modeled using interaction potentials that are functions of maximum adhesion distance, cell geometry (radius), adhesion and repulsion parameters, and distance to other cells. The adhesion function is:

$$\mathbf{F}^{ij}_{\text{cca}} = -C^*_{cca} A_i A_j \nabla\phi_{n_{cca},R_{i,A}+R_{j,A}}(\mathbf{x_j} - \mathbf{x_i}), \tag{21}$$

where C^*_{cca} is the cell-cell adhesion parameter, A_i and A_j are the cell-cell relative adhesion parameters (bounded inclusively between 0 and 1), ϕ is the potential function, n_{cca} a parameter setting the shape of the potential function, and $R_{i,A}$ and $R_{j,A}$ are the maximum adhesion distances of cells i and j respectively. Note that this gives C^*_{cca} units of force. To define the mechanics parameter in PhysiCell, we divide through by ν giving:

$$C_{cca} = \frac{1}{\nu} C_{cca^*} \tag{22}$$

with C_{cca} taking on units of speed, as expected for Equation 20

This is the repulsion function:

$$\mathbf{F}^{ij}_{\text{ccr}} = -C^*_{ccr} \nabla\psi_{n_{ccr},R_i+R_j}(\mathbf{x_j} - \mathbf{x_i}), \tag{23}$$

where C^*_{ccr} is the cell-cell repulsion parameter, n_{ccr} is a parameter setting the shape of the potential function, and R_i and R_j are the cell radii of the two interacting cells i and j. As above with C_{cca*}, we divide C_{ccr*} by ν:

$$C_{ccr} = \frac{1}{\nu} C_{ccr^*} \tag{24}$$

giving C_{ccr} has units of speed.

Finally, PhysiCell uses the following potential functions (note that to compute the velocity updates, only the gradients of the potentials are required):

$$\nabla\phi_{n,R(r)} = \begin{cases} \left(1 - \frac{\mathbf{r}}{R_A}\right)^{n+1} & \text{if } \mathbf{r} \leq R_A \\ \mathbf{0} & \text{otherwise.} \end{cases} \tag{25}$$

for adhesion and:

$$\nabla\psi_{n,R(r)} = \begin{cases} -\left(1-\frac{\mathbf{r}}{R}\right)^{n+1} & \text{if } \mathbf{r} \leq R \\ \mathbf{0} & \text{otherwise.} \end{cases} \tag{26}$$

for repulsion. $\mathbf{r}$ is the distance between the interacting cells' centers, R_A is the sum of i and j's interaction distances, and R is the sum of the two cells' diameters.

7.4 PhysiCell rules

PhysiCell rules is a new extension to PhysiCell [83]. It uses a grammar for mathematical representation of cell-based rules or hypothesis of the conceptual form that an arbitrary number of signals (eg - contact with other cells, a substrate concentration, ECM density) may increase or decrease a cell behavior (eg - cell speed, cell-cell adhesion, ECM production rate). The base form is as follows:

$$b(s) = b_0 + (b_M - b_0)R(s) \tag{27}$$

where b_0 is the base level of a rate or other parameter modifiable at the cell level, b_M is the maximum quantity expected, and $R(s)$ is the functional relationship between the behavior b and signal s. In our examples, we use the default functional form for $R(s)$ - Hill functions. Each Hill function requires a half-maximum saturation value and Hill exponent. As more than one signal may influence a behavior and the influence may be excitatory or inhibitory, Johnson et al. generalize the response of behavior b to a vector of $\mathbf{u}$ and $\mathbf{d}$ up and down signals respectively. These are used to produce the general form of Equation 27:

$$b(\mathbf{u}, \mathbf{d}) = (1 - D)\left((1 - U)b_0 + U \cdot b_M\right) + D \cdot b_M \tag{28}$$

where D and U are the total up and down responses to vectors of signals $\mathbf{u}$ and $\mathbf{d}$.

7.5 Model parameters

In general, parameter values were selected to allow emergent behavior to occur on a reasonable time scale. We performed a joint parameter sweep to determine the cell-cell adhesion and cell speeds using a preliminary version of the collective invasion model. Those initial values were modified for the fibrosis and invasive carcinoma models. Similarly, the fiber realignment and reorientation rates were initially determined through single variable parameter sweep of preliminary versions of the collective invasion model.

The value for oxygen diffusivity is from [84]. Decay and uptake rates, which together set the oxygen diffusion length scales for low cellular density and packed tissue come from [79]. See [62] and [79] for more details. The boundary value for oxygen is set to be typical physioxic conditions of ∼5% of atmospheric oxygen, or 38 mmHg [85].

7.5.1 Fibrosis parameter details

See Tables 4 to 7 for the fibrosis model parameters. Rules are below.

Fibrosis cell rule details

In fibroblast cells:

- Contact with macrophage increases `custom:ECM_production_rate` (ECM density production) rate from 0.0001 min^{-1} towards 0.001 min^{-1} with a Hill response, with half-maximum 0.1 contacts and Hill power 10.

In dead cells:

- None

In macrophage cells:

- Contact with dead cell increases `inflammatory_signal` secretion from 0 towards 10 min^{-1} with a Hill response, with half-maximum 0.1 contacts and Hill power 10.
- Volume decreases `phagocytose dead cell` from 0.0005 min^{-1} towards 0.0001 min^{-1} with a Hill response, with half-maximum 2494 μm^3 and Hill power 10.

7.5.2 Invasive carcinoma parameter details

See Tables 8 to 11 for the invasive carcinoma parameters. Rules are below.

Invasive Carcinoma Cell rule details

In fibroblast cells:

- Contact with cancer cell decreases `custom:rules_based_speed_multiplier` (cell speed) from 1 towards 0.5 with a Hill response, with half-maximum 0.1 contacts and Hill power 4.

In cancer cells:

- contact with fibroblast decreases `inflammatory_signal` secretion from 50 min^{-1} towards 1 with a Hill response, with half-maximum 0.5 contacts and Hill power 4.

Parameter	Value
Adhesion strength	Fibroblast and macrophage - 5.0 μm/min, Dead cell - 10.0 μm/min
Repulsion strength	25.0 μm/min
Base cell speed	Fibroblast and macrophage - 0.5, Dead cell - 0.0
ρ_{ideal}	All - 0.5
ρ_h	All - 1.0
ρ_l	All - 0.0
ECM sensitivity	All - 0.0
Debris secretion rate	Dead cells - 1.0 min^{-1}
Debris target	Dead cells - 10
Debris uptake	Macrophages - 1.0 min^{-1}
Inflammatory signal secretion rate	Macrophages - see Fibrosis rules
Inflammatory signal target	Macrophages - 1.0
Rate of proliferation	All - 0 min^{-1}
Rate of death	All - 0 min^{-1} (dead cells begin the simulation already in a death process)
Chemotactic bias	Fibroblasts and macrophages - 0.5
Persistence time	10 min
Fiber realignment rate (rate of change in anisotropy)	Fibroblast - 0.004 min^{-1}
Fiber reorientation rate	Fibroblast - 4 min^{-1}
ρ_{target}	Macrophages - 0.5, Fibroblast - 1.0
Density modification rate	Macrophages - 0.0 min^{-1}, Fibroblast - See Fibrosis rules

Table 4: Cell-level parameters specific to the fibrosis model.

Parameter	Value
Inflammatory signal diffusivity	1,000 μm^2/min
Inflammatory signal decay constant	1.0 min^{-1}
Debris diffusivity	1.0 μm^2/min
Debris decay constant	0.0 min^{-1}
Boundary condition type	No flux

Table 5: Biotransport and chemical microenvironment parameters for fibrosis model.

Parameter	Value
Initial anisotropy	0
Initial density	0.5
Initial orientation	random

Table 6: ECM initial conditions and remodeling parameters for fibrosis model.

Parameter	Value
Initial region of distressed/dead cell radius	175 μm
Computational domain size	1600 μm by 1600 μm
Pre-mechanics microenvironment conditioning duration	10 min

Table 7: Tissue level parameters for fibrosis model.

- Contact with fibroblast decreases `adhesive affinity to cancer cell` from 1 towards 0.25 with a Hill response, with half-max 0.1 and Hill power 4.
- Contact with fibroblast decreases `cell-cell adhesion` from 0.5 towards 0.25 with a Hill response, with half-max 0.1 contacts and Hill power 4.

Parameter	Value
Adhesion strength	Cancer cell - 0.5 μm/min, Fibroblast - see Invasive carcinoma rules
Repulsion strength	6.25 μm/min
Base cell speed	Cancer cell - 0.25, Fibroblast - see Invasive carcinoma rules
ρ_{ideal}	Both - 0.5
ρ_h	Both - 1.0
ρ_l	Both - 0.0
Oxygen uptake	Both - 10 mmHg/min
ECM sensitivity	Cancer cell - 1.0, Fibroblast - 0.0
Inflammatory signal uptake	Fibroblast - 1.0 min^{-1}
Inflammatory signal secretion rate	Cancer cell - See Invasive carcinoma rules
Inflammatory signal target value	Cancer cell - 1.0
Rate of proliferation	Both - 0 min^{-1}
Rate of death	Both - 0 min^{-1}
Chemotactic bias	Fibroblasts - 0.95, cancer cells - 0.5
Persistence time	10 min
Fiber realignment rate (rate of change in anisotropy)	Fibroblast - 0.02 min^{-1}
Fiber reorientation rate	Fibroblast - 4 min^{-1}
ρ_{target}	Both - 0.5
Density modification rate	Cancer cell - 0 min^{-1}, Fibroblast - 0.001 min^{-1}

Table 8: Cell-level parameters specific to the invasive carcinoma model.

Parameter	Value
Oxygen diffusivity	100,000 μm^2/min
Oxygen decay constant	0.1 mmHg oxygen/min
Oxygen boundary condition type	Mixed
Oxygen boundary condition value	38 mmHg oxygen (Dirichlet), 0 mmHg/min^{-1}
Inflammatory signal diffusivity	1000 μm^2/min
Inflammatory signal decay constant	0.1 mmHg oxygen/min
Inflammatory signal boundary condition type	No flux

Table 9: Biotransport and chemical microenvironment parameters for invasive carcinoma model.

7.5.3 Collective migration parameter details

See Tables 12 to 15 for collective migration parameters. Note there are no cell rules for this model.

Parameter	Value
Initial anisotropy	0
Initial density	0.0 in lumen, 1.0 in barrier, 0.5 outside of duct
Initial orientation	random

Table 10: ECM initial conditions and remodeling parameters for all invasive carcinoma model.

Parameter	Value
Initial tumor radius	175 μm
Computational domain size	1600 μm by 1600 μm
Pre-mechanics microenvironment conditioning duration	10 min

Table 11: Tissue level parameters for invasive carcinoma model.

Parameter	Value	Range
Adhesion strength	varies	0, 10 μm/min
Repulsion strength	25.0 μm/min	-
Base cell speed	varies	0.1, 0.5, 0.8 μm/min
ρ_{ideal}	0.5	-
ρ_h	1.0	-
ρ_l	0.0	-
ECM sensitivity	varies	0.0 (no reading), 1.0 (all other simulations), 0.004 min^{-1}, 0 for leaders (all simulations)
Oxygen uptake	10 mmHg/min	-
Rate of proliferation	0 min^{-1}	-
Rate of death	0 min^{-1}	-
Chemotactic bias	Leaders - 0.95, followers - dynamic	-
Persistence time	10 min	-
Fiber realignment rate (rate of change in anisotropy)	varies	0.0 (no writing), 0.001 (loss of collective migration scenario), 0.004 min^{-1}, 0 for followers (all simulations)
Fiber reorientation rate	varies	0.0 (no writing), 1 (loss of collective migration scenario), 4 min^{-1}, 0 for followers (all simulations)
ρ_{target}	0.5	-
Density modification rate	0.0	-

Table 12: Cell-level parameters specific to the collective migration model. Unless otherwise stated, parameters are at default values.

Parameter	Value
Oxygen diffusivity	100,000 μm^2/min
Oxygen decay constant	0.1 mmHg oxygen/min
Boundary condition type	Dirichlet
Boundary condition value	38 mmHg oxygen

Table 13: Biotransport and chemical microenvironment parameters for collective migration model.

Parameter	Value
Initial anisotropy	0
Initial density	0.5
Initial orientation	random

Table 14: ECM initial conditions for all collective migration simulations.

Parameter	Value
Initial organoid radius	175 μm
Computational domain size	1600 μm by 1600 μm
Pre-mechanics microenvironment conditioning duration	10 min
Cell fraction of leaders	0.05

Table 15: Tissue level parameters for collective migration model.

7.6 Links to supplemental videos

SM Video 1: Writing to ECM (local microstructure remodeling) - Cell-based ECM reorientation (Figure 2a)

SM Video 2: Reading ECM (contact guidance) - Circular ECM with no gradient (Figure 2b)

SM Video 3: Reading ECM (contact guidance) - Circular ECM with chemical gradient (Figure 2c)

SM Video 4: Wound healing and fibrosis (Figure 3)

SM Video 5: Basement membrane degradation and transition of *in situ* carcinoma to invasion (Figure 4)

SM Video 6: Writing signals to ECM only (no reading/contact guidance) (Figure 5a)

SM Video 7: Reading signals from ECM only (no writing/microscale remodeling) (Figure 5b)

SM Video 8: Local microstructure remodeling (reading) and writing (contact guidance) leads to stigmergy (Figure 5c)

SM Video 9: Leader-follower - instant remodeling - higher cell speed (Figure 6a)

SM Video 10: Leader-follower - instant remodeling - medium cell speed (Figures 6b, 7a, SM4a)

SM Video 11: Leader-follower - instant remodeling - lower cell speed (Figure 6c)

SM Video 12: Collective migration - Non-instant signal writing (Figure 7b)

SM Video 13: Reading ECM (contact guidance) - split ECM pattern with chemical gradient (SM Figure 3)

SM Video 14: Collective migration - Loss of collective migration due to decreased remodeling rates (SM Figure 4b)

7.7 Supplemental Figures

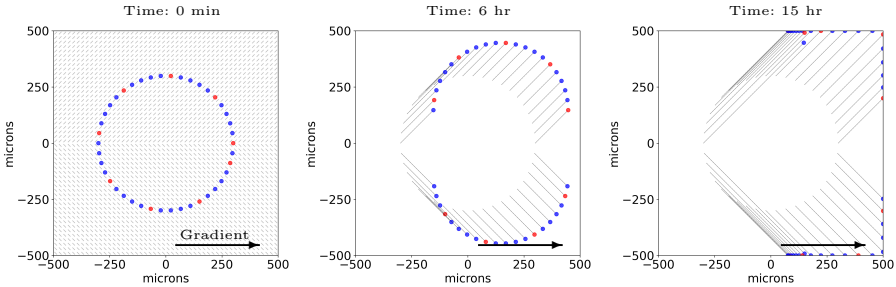

Supplementary Figure 3: **Highlight of individual aspects of the ECM-cell interactions: ECM orientation and cell chemotaxis** A combination of cues directing cell motility: ECM orientation (45° in the top of the domain and -45° in the bottom) and chemical gradient (to the right). The small black arrows trailing the cells show the positional history of each cell. The cell position is marked every six simulated minutes. Red and blue cells are identical; the coloring was added only for visual contrast. This is available as a video. See link the to video here.

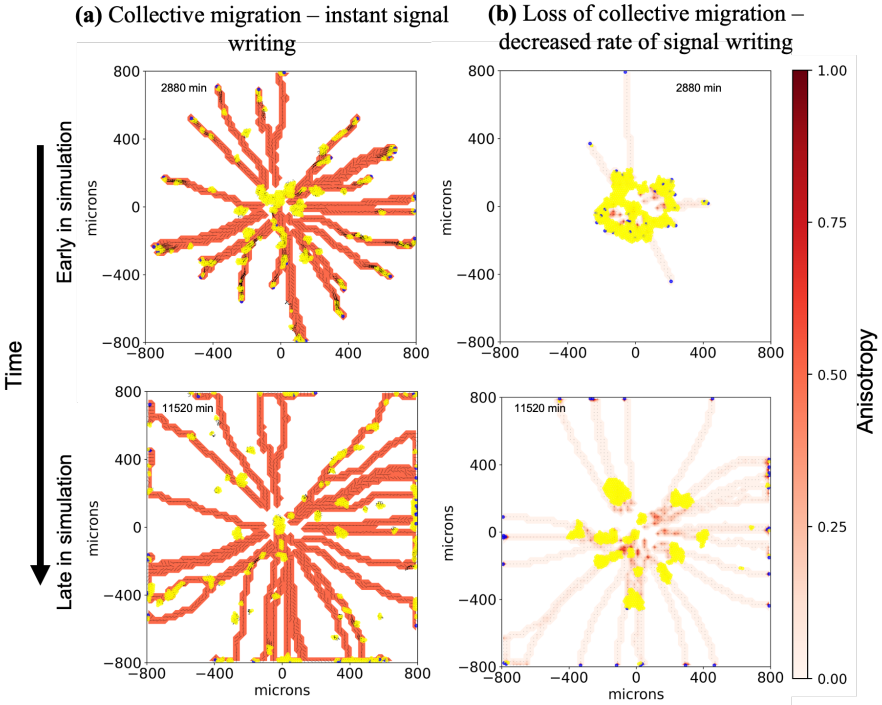

Supplementary Figure 4: **Collective migration requires sufficiently fast remodeling parameters a** with instantaneous ECM remodeling contrasts with with **b** which has relaxed the instantaneous signal writing and has remodeling rates slower than that in Figure 7b. Fiber realignment rate: 0.001 min^{-1}, fiber reorientation rate: 1 min^{-1}. Videos are available. See the following links 6b and SM4b..